Kink Oscillations in Solar Coronal Loops with Elliptical Cross Sections. I. The Linear Regime

Mingzhe Guo[1] , Bo Li[1] , and Tom Van Doorsselaere[2]

[1] Shandong Provincial Key Laboratory of Optical Astronomy and Solar-Terrestrial Environment, Institute of Space Sciences, Shandong University, Weihai 264209, People's Republic of China; m.guo@sdu.edu.cn
[2] Centre for Mathematical Plasma Astrophysics, Department of Mathematics, KU Leuven, B-3001 Leuven, Belgium

Abstract

The cross sections of solar coronal loops are suggested to be rarely circular. We examine linear kink oscillations in straight, density-enhanced, magnetic cylinders with elliptical cross sections by solving the three-dimensional magnetohydrodynamic equations from an initial-value-problem perspective. Motivated by relevant eigenmode analyses, we distinguish between two independent polarizations, one along the major axis (the M-modes) and the other along the minor one (the m-modes). We find that, as happens for coronal loops with circular cross sections, the apparent damping of the transverse displacement of the loop axis is accompanied by the accumulation of transverse Alfvénic motions and the consequent development of small scales therein, suggesting the robustness of the concepts of resonant absorption and phase mixing. In addition, two stages can in general be told apart in the temporal evolution of the loop displacement: a Gaussian time dependence precedes an exponential one. For the two examined density ratios between loops and their surroundings, the periods of the M-modes (m-modes) tend to increase (decrease) with the major-to-minor-half-axis ratio, and the damping times in the exponential stage for the M-modes tend to exceed their m-mode counterparts. This is true for the two transverse profiles we examine. However, the relative magnitudes of the damping times in the exponential stage for different polarizations depend on the specification of the transverse profile or the density contrast. The applications of our numerical findings are discussed in the context of coronal seismology.

Unified Astronomy Thesaurus concepts: Solar corona (1483); Magnetohydrodynamics (1964); Solar coronal waves (1995)

Supporting material: animations

1. Introduction

Cyclic transverse displacements of solar coronal loops have been observed frequently and in great detail and have been customarily interpreted as kink waves that are collectively supported therein (see, e.g., Nakariakov & Verwichte 2005; Banerjee et al. 2007; De Moortel & Nakariakov 2012; Nakariakov et al. 2016b; Wang 2016, for recent reviews). While evidence for propagating kink waves has been offered by instruments such as the Coronal Multi-Channel Polarimeter (CoMP; e.g., Tomczyk et al. 2007; Tomczyk & McIntosh 2009), most of the transverse motions have been found to be compatible with standing kink waves (or kink oscillations in other words) ever since they were first imaged by the Transition Region and Coronal Explorer (TRACE; Aschwanden et al. 1999 and Nakariakov et al. 1999) and subsequently by Hinode (Erdélyi & Taroyan 2008; Ofman & Wang 2008; Van Doorsselaere et al. 2008), the Solar TErrestrial RElations Observatories (STEREO; Verwichte et al. 2009), and the Solar Dynamics Observatory/Atmospheric Imaging Assembly (SDO/AIA; e.g., Aschwanden & Schrijver 2011; White & Verwichte 2012). Two regimes exist in kink oscillations. The loop displacements associated with the so-called decayless kink oscillations barely exceed the loop diameter and experience little damping (e.g., Tian et al. 2012; Wang et al. 2012; Anfinogentov et al. 2013; Nisticò et al. 2013; Anfinogentov & Nakariakov 2019). In addition, they tend not to be connected with eruptive events such as flares or coronal mass ejections (e.g., Anfinogentov et al. 2015). This then raises the question as to whether the continuous energy supply, necessary

for maintaining a nearly constant oscillatory behavior and most likely connected with footpoint motions, comes in a quasi-steady (e.g., Nakariakov et al. 2016a), nearly monochromatic (e.g., Karampelas et al. 2017; Guo et al. 2019a; see also Antolin et al. 2016), or random manner (Afanasyev et al. 2020). Decaying kink oscillations, on the other hand, are of larger amplitude and are almost always associated with lower coronal eruptions (e.g., Zimovets & Nakariakov 2015; Nechaeva et al. 2019). They tend to damp in several cycles, a feature evident in both individual measurements (e.g., Aschwanden et al. 1999; Nakariakov et al. 1999) and statistical surveys (e.g., Verwichte et al. 2013; Goddard et al. 2016; Nechaeva et al. 2019).

Decaying kink oscillations, the focus of the present study, have been routinely exploited from the perspective of coronal seismology since their discovery (see, e.g., the early review by Roberts 2000). This is understandable because the measured periods can be inverted for the magnetic field strength in coronal loops, which is difficult to routinely measure otherwise (Nakariakov & Ofman 2001; see also the reviews by, e.g., Nakariakov & Verwichte 2005 and Nakariakov et al. 2016b). The measured damping times have proven equally useful given that the damping is largely accepted to result from the resonant conversion of the kink energy to localized Alfvén waves, a concept originally proposed to account for coronal heating (e.g., Ionson 1978; Wentzel 1979; Hollweg & Yang 1988) and later invoked for seismological purposes (Goossens et al. 2002; Ruderman & Roberts 2002; Aschwanden et al. 2003; Van Doorsselaere et al. 2004; see also the review by Goossens et al. 2011 and references

therein). When put into practice, the theory of this "resonant absorption" enables one to constrain the transverse inhomogeneity length scale of the loop density either analytically (e.g., Goossens et al. 2008) or largely numerically (e.g., Arregui et al. 2007; Soler et al. 2014). Note that the relevant theoretical analysis is usually conducted from the eigenvalue problem perspective (see, e.g., the review by Goossens et al. 2011). It then follows from the pertinent solution to the initial-value problem that the damping rate pertains to the asymptotic stage where the system has evolved for a time much longer than $P_k/2\pi$ and the wave damping is exponential in time, where P_k is the kink period (e.g., Ruderman & Roberts 2002, 2006). It is fortunate that an exponential damping profile is usually present in observations of loop oscillations, but it is unfortunate that the damping times thus measured, together with the measured periods, allow one to constrain the equilibrium loop parameters only to a one-dimensional curve in the three-dimensional (3D) parameter space formed by the longitudinal Alfvén time, the density contrast between the loop and its ambient surroundings, and the transverse density length scale (e.g., Arregui et al. 2007; Goossens et al. 2008; Chen et al. 2015; see also the comments on the underdetermined nature of the inversion problem by Arregui & Goossens 2019).

The underdetermined situation in seismological practices has been shown to improve when one incorporates the information in the transitory phase, namely the phase before the system evolves into the asymptotic stage. This was first noted in the numerical studies on propagating kink waves by Pascoe et al. (2012), where the authors found that resonant absorption operates in this case as well, but in general the spatial damping profile is Gaussian-like in the first couple of wavelengths before becoming an exponential one. The numerical findings soon received the theoretical support from Hood et al. (2013). In addition, a temporal damping profile, in which a Gaussian time dependence precedes an exponential one, is expected for kink oscillations if one translates the spatial behavior of propagating waves to the temporal behavior of standing waves with the aid of the axial group speed (Pascoe et al. 2013). Theoretically speaking, this expectation was corroborated by analytical (Ruderman & Terradas 2013) and numerical studies (e.g., Soler & Terradas 2015; Magyar & Van Doorsselaere 2016). More importantly, observational evidence for the Gaussian damping was indeed found for decaying kink oscillations (Pascoe et al. 2016b). As such, the damping times in the Gaussian stage become an additional measurable that further constrains the loop parameters (e.g., Pascoe et al. 2016c, 2018). Recently, the damping profiles including the Gaussian stage in coronal loops with various density profiles were provided in a look-up table, which can be used for seismology (Pascoe et al. 2019).

The theories behind all of the aforementioned seismological applications have assumed that coronal loops are monolithic density enhancements that are embedded in otherwise uniform ambient and straight magnetic flux tubes with a constant circular cross section everywhere (e.g., Goossens et al. 2011). This geometrical assumption actually involves two interconnected aspects: the loop shape and the loop cross-sectional properties. The loop shape, namely the morphology of the loop axis projected onto the plane of the sky, is certainly curved rather than straight (see, e.g., the review by Aschwanden 2009, and references therein). Considerably less certain are the cross-sectional properties, by which we mean the spatial variation along the loop of the surface enclosing the density enhancement. While stereoscopic observations with, say, the twin STEREO spacecraft can in principle place constraints on this aspect (e.g., see the review by Aschwanden 2011), a practical implementation is not straightforward, the primary issue being the optical thinness of the corona in the relevant passbands (see, e.g., Malanushenko & Schrijver 2013). As for spectroscopic measurements, issues associated with determining the filling factors and the loop background further complicate the problem (e.g., Kucera et al. 2019, and references therein). A common practice is then to employ some modeled coronal magnetic fields to examine the geometry of magnetic flux tubes. Note that, by construction, the cross section is allowed to be prescribed at only one location but needs to be computed elsewhere (e.g., Ruderman 2009). While it is statistically true that cross-sectional areas tend to vary more strongly in current-free fields than in force-free but non-current-free fields (e.g., Wang & Sakurai 1998; Klimchuk et al. 2000; López Fuentes et al. 2006, and references therein), there seems to be no definitive conclusion as to the cross-sectional behavior of individual flux tubes. Depending on the choice of the field model, even if the cross-sectional area of selected flux tubes may not vary too much (e.g., Malanushenko & Schrijver 2013), the dimensions along different directions intersecting the cross sections may do so (e.g., Wang & Sakurai 1998). It is even possible, at least for thin flux tubes in planar, current-free fields, that both the shape and dimensions of flux-tube cross sections are preserved (Ruderman 2015).

Now return to kink oscillations in coronal loops. With the realistic features of magnetic flux tubes in mind, it should be ideal for one to set up an equilibrium that addresses simultaneously a curved loop shape and a position-dependent noncircular cross section. A number of numerical studies have indeed been devoted to this purpose (e.g., McLaughlin & Ofman 2008; Selwa & Ofman 2010; Selwa et al. 2011b; Magyar & Nakariakov 2020). However, one issue associated with this practice is that the wave behavior is at best marginally analytically tractable (Ruderman 2009), thereby making it difficult to draw a definitive conclusion on such issues as the relative importance of wave leakage versus resonant absorption for damping kink oscillations. It is then no surprise to see that more studies tend to isolate one geometric factor out of many. For instance, a curved loop with a position-independent circular cross section has been rather extensively examined (see the review by Van Doorsselaere et al. 2009 for earlier papers, and also De Moortel & Pascoe 2009; Pascoe & De Moortel 2014). Likewise, a straight loop with a position-independent elliptic cross section has also received much attention given that it permits a largely analytical eigenmode analysis (e.g., Ruderman 2003; Erdélyi & Morton 2009; Morton & Ruderman 2011; also G. Verth et al. 2020, private communications). It was shown that this geometry, although different from the classical one only in replacing a circular with an elliptic cross section, brings forth the important difference that now kink oscillations polarized along the major and minor axes are no longer degenerate. Nonetheless, resonant absorption was found to operate for kink oscillations with these two independent polarizations (Ruderman 2003, hereafter R03).

This manuscript is intended to examine kink oscillations in active region (AR) loops modeled as straight, density-enhanced flux tubes with elliptic cross sections by numerically solving

the 3D ideal MHD equations. Some justifications for our approach seem necessary at this point. First, while our equilibrium is similar to the one in the eigenmode analysis by R03, examining kink oscillations from the initial-value-problem perspective will allow us to address a number of additional questions. For instance, can a Gaussian damping envelope be identified before an exponential one, as happens for loops with circular cross sections? What will be the seismological applications if both phases occur in general, and will it be possible to infer the aspect ratio of the cross sections in particular? Second, neglecting the curvature of the loop axis means that the wave damping will be solely due to resonant absorption taking place primarily in the neighborhood of the loop boundary. This can be only partially justified because while there are studies suggesting that resonant absorption dominates such curvature-related factors as wave leakage or additional resonant absorption taking place in the ambient corona (Terradas et al. 2006a), there are also studies that indicate otherwise (e.g., McLaughlin & Ofman 2008; Selwa et al. 2011a). Having said that, loop curvature is expected to influence the periods to a lesser degree, at least when a position-independent circular cross section is adopted for the modeled loops (Terradas et al. 2006a; see also the review by Van Doorsselaere et al. 2009). Now thinking about loops for which the loop axis is curved but a position-independent elliptic cross section can be maintained, our results regarding the periods are likely to apply, even though the computed damping rates need to be treated with some caution.

This paper is organized as follows. Section 2 details the specification of our equilibrium configuration and our numerical implementation. The numerical results are then described in Section 3, followed by some rather detailed discussions on their potential seismological applications in Section 4. Section 5 summarizes the present study, ending with some concluding remarks.

2. Model Formulation and Numerical Methods

2.1. Equilibrium Setup

We work in the framework of ideal MHD throughout, for which the primary dependents are the mass density ρ, velocity $\boldsymbol{v}$, magnetic field $\boldsymbol{B}$, and thermal pressure p. Assuming an electron–proton plasma, one then relates the mass density to the electron number density N through $\rho = Nm_p$ with m_p being the proton mass. Likewise, the thermal pressure is related to the electron temperature T via $p = 2Nk_B T$ where k_B is the Boltzmann constant.

We start with constructing an equilibrium for which all physical parameters are denoted by a subscript 0. A Cartesian coordinate system (x, y, z) is adopted throughout, and the equilibrium magnetic field $\boldsymbol{B}_0$ is assumed to be everywhere in the z-direction. We model a coronal loop as a static, field-aligned density enhancement, for which the axis is aligned with the z-axis and the ambient corona is homogeneous. This loop is of length L, as follows from the assumption that the loop is bounded at both $z = 0$ and $z = L$ by two photospheres. The equilibrium parameters are assumed to be structured only in the transverse directions. Let the subscripts i and e denote the equilibrium parameters at the loop axis and far from the loop, respectively. We then assume that ρ_0 takes the form

$$\rho_0(x, y) = \rho_e + (\rho_i - \rho_e)f(x, y), \qquad (1)$$

which describes a density profile varying continuously from the internal value at the axis to the external value in the sufficiently far ambient medium. This variation is realized through the function f, which depends on the transverse coordinates x and y through an intermediate variable $\bar{r}$ as

$$f(x, y) \equiv f(\bar{r}) = \frac{1}{1 + \bar{r}^\alpha}, \qquad (2)$$

with

$$\bar{r} = \sqrt{\left(\frac{x}{a}\right)^2 + \left(\frac{y}{b}\right)^2}. \qquad (3)$$

We further assume that $a \geqslant b$. As such, $f(x, y)$ yields an elliptic cross section with a mean major (minor) half-axis being a (b). Furthermore, the parameter α characterizes how steep this f varies. Instead of specifying the distribution of the pressure, we assume that the equilibrium electron temperature (T_0) follows the same spatial dependence as the mass density. The thermal pressure $p_0(x, y)$ is then readily derived, and the magnetic field strength B_0 follows from the transverse force balance,

$$p_0(x, y) + \frac{B_0^2(x, y)}{2\mu_0} = p_i + \frac{B_i^2}{2\mu_0}, \qquad (4)$$

where μ_0 is the magnetic permeability in free space.

The equilibrium configuration is fully determined once we specify the geometrical parameters (L, a, b, and α) and the physical parameters (ρ_i, ρ_e, T_i, T_e, and B_i). Alternatively, these parameters can also be grouped into a set of dimensional parameters [b; ρ_i, T_i; B_i] and a set of dimensionless ones [L/b, a/b, α; ρ_i/ρ_e, T_i/T_e]. Evidently, there are too many parameters to explore with 3D simulations, and therefore we choose to fix many. To be specific, we fix the minor half-axis (b) at 1000 km, the length-to-minor-half-axis ratio (L/b) at 50, and the steepness parameter α at 5. The electron temperature at the loop axis T_i is taken to be 1.4 MK, and the internal-to-external temperature ratio T_i/T_e is fixed at 2. In addition, we fix the internal density ρ_i such that it corresponds to an electron number density of 10^9 cm^{-3}. The magnetic field strength at the loop axis (B_i) is taken to be 15 G, resulting in a plasma β of $\beta_i = 0.043$ and an Alfvén speed of $v_{Ai} = 1035$ km s^{-1}. We are left with the aspect ratio (a/b) and the density ratio ρ_i/ρ_e varying. The parameters we either fix or allow to vary are largely typical of warm active-region loops (e.g., see the review by Reale 2014), even though the steepness parameter is known to be difficult to observationally constrain (e.g., Aschwanden et al. 2003; Pascoe et al. 2018). For illustration purposes, Figure 1 shows an equilibrium loop corresponding to the combination of [a/b, ρ_i/ρ_e] = [2, 2]. The loop boundary is shown by the shaded surface, and the filled contours at the loop apex represent the transverse distribution of the mass density.

2.2. Numerical Setup

We examine the properties of the fundamental kink modes supported by the considered equilibrium by numerically following the response of the equilibrium to an initial velocity perturbation $\boldsymbol{v}(x, y, z; t = 0)$. However, following R03, we know a priori that now the kink modes correspond to two independent polarizations as far as the velocity field is concerned. This means that two different types of initial
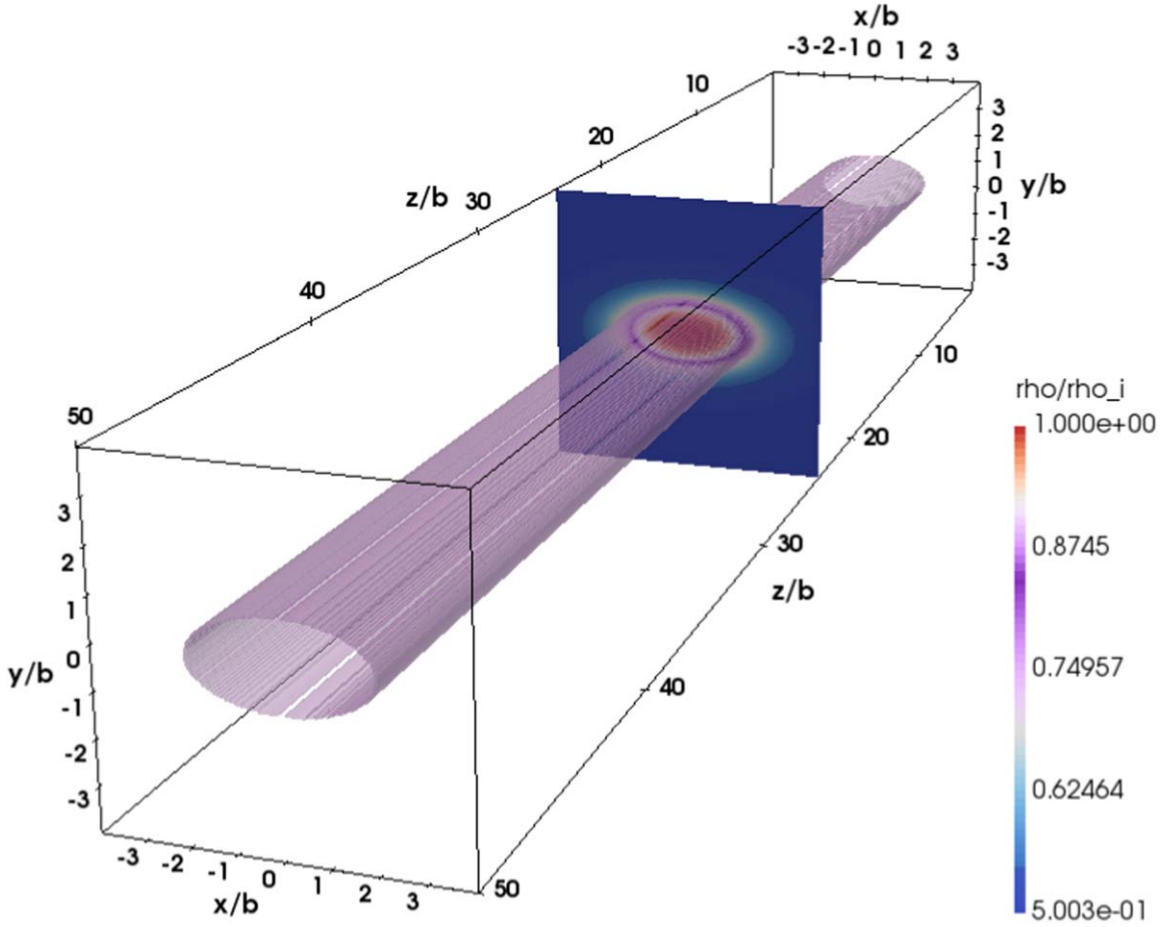
Figure 1. Illustration of the equilibrium configuration involving a straight coronal loop with elliptic cross sections realized through Equation (2). The loop boundary with a mean major half-axis a and minor half-axis b is given by the shaded surface. The filled contours are for the distribution of the mass density in the transverse plane. For illustration purposes, here we adopt an aspect ratio $a/b = 2$, an internal-to-external density ratio $\rho_i/\rho_e = 2$, a steepness parameter $\alpha = 5$, and a length-to-minor-half-axis ratio $L/b = 50$.

perturbations need to be distinguished from the outset. Accordingly, different setups for the numerical grid are necessary to save computational costs. For ease of description, let the modes polarized in the direction of the major (minor) axis be denoted by the M-modes (m-modes). In addition, recall that the major and minor axes are aligned with the x- and y-directions, respectively.

To excite fundamental M-modes, we introduce an initial perturbation of the form

$$\boldsymbol{v}(x, y, z; t = 0) = v_0 f(x, y)\sin\left(\frac{\pi z}{L}\right)\hat{x}. \qquad (5)$$

Here, v_0 denotes the amplitude of the perturbation, and $\hat{x}$ represents the unit vector in the x-direction. In addition, $f(x, y)$ has been described by Equation (2) and is adopted here to avoid introducing additional parameters that characterize the spatial profile of initial perturbations. The symmetric properties of the kink modes in this situation allow us to consider only a quarter of the nominal computational domain of $(-\infty, \infty) \times (-\infty, \infty) \times [0, L]$. In practice, we adopt a simulation domain of $[-15, 15]\, b \times [0, 15]\, b \times [0, L/2]$, and we apply symmetric boundary conditions at both $y = 0$ and $z = L/2$ (e.g., Antolin et al. 2015; Karampelas et al. 2017). Our base computations employ 25 uniform cells in the z-direction, but we adopt 590 (175) nonuniformly spaced cells in

the x (y) direction. To be specific, along the x-direction, 480 grid points are uniformly distributed for $-8b \leqslant x \leqslant 8b$, beyond which a stretched grid is used. Likewise, 120 uniform grids are adopted in the y-direction in the interval $0 \leqslant y \leqslant 4b$, outside which a stretched grid is employed. This grid system is constructed primarily to make our computations less numerically expensive, with the uniform portion adopted to adequately capture the wave dynamics. The resulting spatial resolution reaches up to $\sim b/30 = 33$ km in both directions.

To excite fundamental m-modes, we introduce an initial perturbation identical in form to Equation (5) except that $\hat{x}$ is replaced with $\hat{y}$. We adopt a simulation domain of $[0, 15]\, b \times [-15, 15]\, b \times [0, L/2]$ and apply symmetric boundary conditions at both $x = 0$ and $z = L/2$. In our base computations, the grid setup in the z-direction is identical to the M-mode case. However, now 295 and 350 nonuniformly distributed cells are used in the x- and y-directions, respectively. We employ a uniform grid of 240 (240) points in the interval $0 \leqslant x \leqslant 8b$ ($-4b \leqslant y \leqslant 4b$) but use a stretched grid in the rest of the domain. This choice ensures the same highest resolution as in the base computations for the M-modes.

The rest of the numerical implementation is common to both polarizations. The amplitude of the initial perturbation v_0 is taken to be 4 km s^{-1} (or equivalently $\sim 0.0039\, v_{Ai}$) to avoid complications associated with nonlinearities. Regarding the

boundary conditions at the loop footpoint ($z = 0$), both v_x and v_y are set to vanish, while v_z, B_x, and B_y follow the zero-gradient condition. The remaining physical variables are fixed at their initial values here. Outflow boundary conditions are applied to all lateral boundaries. We then solve the time-dependent, ideal MHD equations with the PLUTO code (Mignone et al. 2007). Following the reconstruct–solve–average strategy, we choose the piecewise parabolic scheme for reconstruction, the HLLD Riemann solver for computing the numerical fluxes, and the second-order Runge–Kutta method for time marching.

3. Numerical Results

We examine a number of combinations of a/b and ρ_i/ρ_e. The aspect ratio (a/b) varies between 1 and 3, a range compatible with the spectroscopically derived values (Kucera et al. 2019). Alternatively, the deviation of a cross section from a circular one can also be measured in terms of flattening $\xi = 1 - b/a$. For an $a/b = 3$, the flattening is $\xi = 2/3$. Given the computational costs of 3D simulations, we examine only two values of the density ratio (ρ_i/ρ_e), one being 2 and the other being 8. On the one hand, these two density ratios lie almost at the extreme of the observed range for typical active-region loops (2–10; e.g., Aschwanden et al. 2004) and therefore are likely to be representative of low- and high-density ratios. On the other hand, as can be deduced from R03, the damping times for the m-modes tend to exceed those for the M-modes when $\rho_i/\rho_e \lesssim 5$, whereas this trend is reversed when $\rho_i/\rho_e \gtrsim 5$. Note that our prescription of the transverse distribution (Equation (2)) is different from R03, where a linear profile is implemented with the elliptic coordinates (Equation (A3)). In addition, R03 worked in the framework of zero-β MHD and adopted the thin-tube-tube-boundary (TTTB) approximation for analytical tractability. The loops we examine are rather long ($L = 50\,b$), making a/L still rather small for the extreme value of $a/b = 3$ and hence the thin-tube (TT) approximation likely to hold. However, adopting an $\alpha = 5$ means that our transverse profiles are not that steep to satisfy the thin-boundary (TB) approximation. Note also that R03 performed an eigenmode analysis, meaning that the damping times therein apply to the exponential stage. In contrast, we approach the problem from an initial-value-problem perspective and are therefore able to address whether the damping envelopes of the oscillatory signals are purely exponential. The net result is that it is not that informative to quantitatively contrast our numerical results (say, the damping times in the exponential stage and the periods) with the analytical expectations from R03. However, a qualitative comparison of the dependence of these parameters on a/b and ρ_i/ρ_e can still be conducted.

At this point, one may question why we choose not to examine the linear transverse profile in R03 from the outset? In fact, we have experimented with this linear profile, and we examined the same two density ratios but a range of a/b that is only up to 1.4. The pertinent results are presented in the appendix, which focuses on steep profiles such that the TB approximation holds. Basically we find that a Gaussian stage can be seen in addition to an exponential one in the damping envelopes. In addition, a rather close agreement is found between R03 and what we derive for the damping times in the exponential stage and the periods. On the one hand, this agreement can be seen as a validation of our numerical

approach. On the other hand, it suggests that the qualitative difference between our results and R03, if any, is unlikely to result from the small values of plasma β in our numerical implementations. The reason for us not to examine the R03 profile in the main text is then twofold. First, our profile is as worth examining as the R03 profile, given the difficulty of constraining observationally the specific form of the transverse profiles (e.g., Arregui & Goossens 2019, and references therein). Second, examining the R03 profile is more computationally expensive. As detailed in the appendix, a rather fine grid is needed to resolve the transverse inhomogeneity even for an a/b as modest as 1.4 if we insist on testing the TB results. The grid resolution is even more demanding for larger values of a/b, only for which the difference in, say, the periods for modes with different polarizations become substantial. If we leave aside the TB consideration, then there will be no analytical expectations as happens for the profile given in Equation (2).

Now let us start with our examination of the kink oscillations in coronal loops with our prescribed transverse profile by looking at the oscillatory behavior of the M-modes. The upper row of Figure 2 presents the temporal evolution of the x-component of the velocity at the loop apex ($v_{x,\mathrm{apex}} \equiv v_x(0, 0, L/2; t)$) for two density ratios, one being $\rho_i/\rho_e = 2$ (the left column) and the other being 8 (right). Different aspect ratios (a/b) are differentiated with the different colors shown in Figure 2(b). From each time series, we extract the extrema $v_{x,\mathrm{apex}}^{\mathrm{extr}}$ and define the damping envelope $D_M(t)$ as $\ln|v_{x,\mathrm{apex}}^{\mathrm{extr}}(t)|$. This discrete D_M series is given by the asterisks in the lower row. We also fit this series with a three-parameter model

$$D(t) = \begin{cases} A^{\mathrm{G}} - \dfrac{1}{2}\left(\dfrac{t}{\tau^{\mathrm{G}}}\right)^2, & t \leqslant t_s \\[2ex] \left[A^{\mathrm{G}} - \dfrac{1}{2}\left(\dfrac{t_s}{\tau^{\mathrm{G}}}\right)^2\right] - \left(\dfrac{t - t_s}{\tau^{\mathrm{E}}}\right), & t > t_s \end{cases} \quad (6)$$

which is motivated by the studies on kink oscillations in loops with circular cross sections (Pascoe et al. 2016c, and references therein). Equation (6) separates a Gaussian envelope from an exponential one, with the two envelopes characterized by the damping times τ^{G} and τ^{E}, respectively. Note that the switch time (t_s) between the two envelopes is not an independent fitting parameter. Rather, it is defined by $(\tau^{\mathrm{G}})^2/\tau^{\mathrm{E}}$, as inspired by the studies by Hood et al. (2013) and Pascoe et al. (2016c), and has the advantage that $D(t)$ is not only continuous but also smooth at t_s. In practice, this means that the model indeed involves only three independent parameters. The best-fit curves are plotted as the dashed lines in the lower row of Figure 2, where we also indicate the derived values of t_s as the vertical dashed–dotted lines.

All time series in the upper row of Figure 2 start with some sudden reduction of the oscillation magnitudes. Here by "sudden" we mean that this phase persists in a time interval that is of the order of the transverse rather than the longitudinal Alfvén time. As first found in time-dependent simulations by Terradas et al. (2006b), this phase is known as the impulsive leaky phase, during which part of the energy imparted by the initial perturbation is emitted into the ambient medium. In other words, the decrease in the oscillation magnitude is connected to the energy-confinement capability of coronal loops, which in turn depends on the extent to which a loop feels the existence
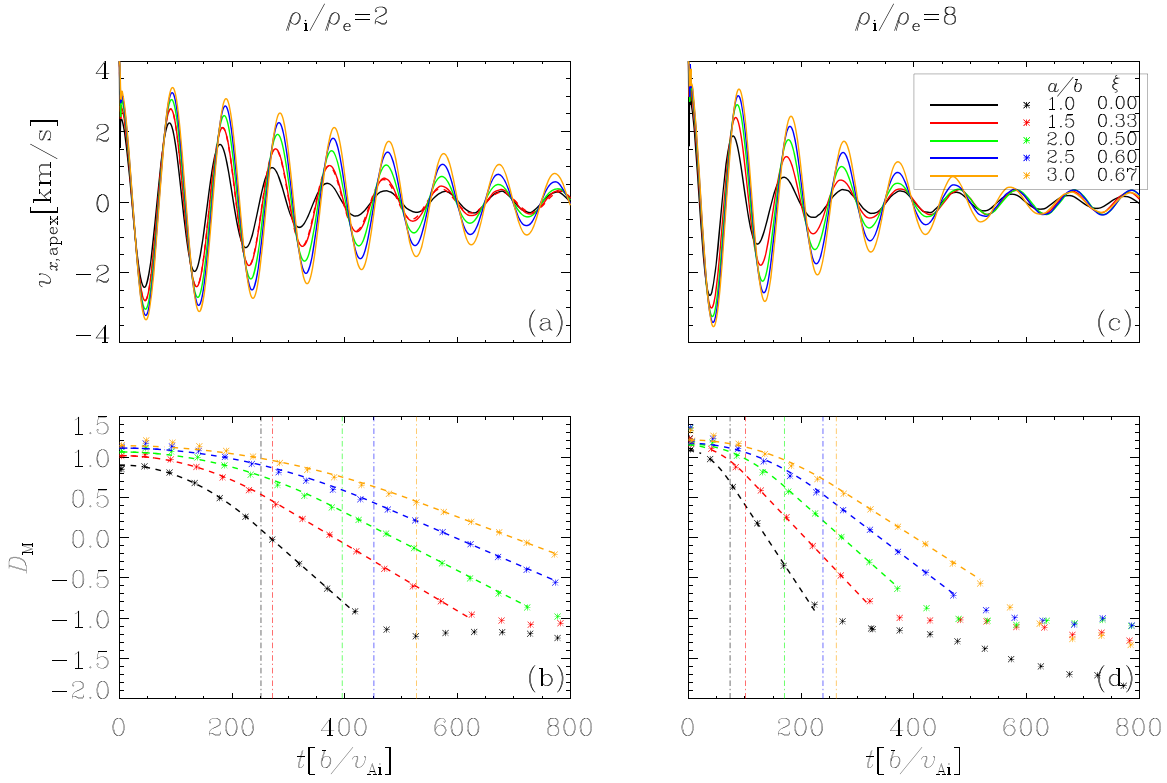
Figure 2. Temporal evolution of the *x*-component of the velocity at the loop apex ($v_{x,\text{apex}}$) for kink oscillations polarized along the major axis (M-modes) supported by loops with elliptic cross sections and transverse profiles described by Equation (2). Two density ratios (ρ_i/ρ_e) are adopted, one being 2 (the left column) and the other being 8 (right). A number of aspect ratios (a/b) are examined as labeled by the different colors. In addition to the time series for $v_{x,\text{apex}}$ itself (the upper row), we also extract the extrema therein and plot the natural logarithms of their absolute values (D_M) in the lower row. The dashed curves represent the best fit to this discrete series with the three-parameter model given in Equation (6), where a Gaussian damping envelope is distinguished from an exponential one. The switch time from one envelope to the other is represented by the vertical dashed–dotted lines. Note that the flattening $\xi = 1 - b/a$ labeled here represents the deviation of a cross section from a circular one.

of its ambient medium. Comparing the curves in different colors in either Figure 2(b) or Figure 2(d), one sees that for a given density ratio (ρ_i/ρ_e), the magnitude of the oscillations tends to increase with the aspect ratio (a/b) in the time interval following the impulsive phase (see, e.g., the asterisks at $t \approx 50\, b/v_{\text{Ai}}$). This is understandable given that the majority of the velocity vectors in the loop region are aligned with the major axis (see Figure 3). With a/b increasing, the velocity field becomes increasingly tangential to the areas where the loop plasmas are in contact with the ambient medium, which decreases the elastic interaction between the loop and its surroundings. Consequently, the loop becomes less aware of its surrounding medium. This heuristic argument, essentially based on inertia considerations, also applies to the observation that, for a given a/b, the oscillations in the first cycle tend to be stronger for a higher density ratio. In this case, a loop is less aware of its ambient medium because the ambient is more tenuous.

The oscillations rather quickly settle into a periodic behavior after the impulsive phase. This periodic behavior is reflected by the nearly constant spacing between adjacent extrema in the lower row of Figure 2, which suggests that a substantial interval can be well fitted with the model given by Equation (6). In particular, a Gaussian damping envelope can indeed be distinguished from an exponential one, even though Equation (6) was motivated by the results for kink oscillations in loops with circular cross sections. However, the oscillations do not weaken indefinitely with time, but rather end up with a rather irregular temporal dependence. This may cause our

fitting procedure to be problematic because if this irregular large-time behavior appears too soon, we will either be unable to discern the exponential envelope or even have too few extrema to discern any envelope at all. While this issue does not arise for the M-modes examined here, it indeed arises for the m-modes to be discussed shortly. But before doing that, let us try to further exploit our time-dependent results to shed more light on the temporal evolution of the system.

Figure 3 shows a few snapshots of a loop system that experiences M-mode oscillations and that corresponds to a combination $[a/b, \rho_i/\rho_e] = [2, 2]$. Shown here is the distribution in the transverse (*x*–*y*) plane of the mass density (filled contours) and the velocity field (arrows) at the loop apex ($z = L/2$). Note that the symmetric properties of M-modes enable us to show only one-half of the system. Note also that the density variations are very weak because of the small amplitude of the initial perturbation, and the density contours are simply intended to outline the loop. Taken from the animation attached to this figure, the snapshots are intended to show the status of the system at a few representative times. In particular, Figure 3(a) shows the initial velocity field, which is entirely in the *x*-direction. One sees from Figure 3(b) that the impulsive leaky phase is almost immediately followed by the development of vortical motions at the outer loop boundary, a characteristic well known for kink oscillations in loops with circular cross sections (see, e.g., Figure 2 in Goossens et al. 2014). On the other hand, Figure 3(c) indicates that the damping of the M-mode, namely the weakening of the motions in the loop interior, is accompanied by the growth of horizontal motions at the loop boundary. This is a well-known signature of resonant
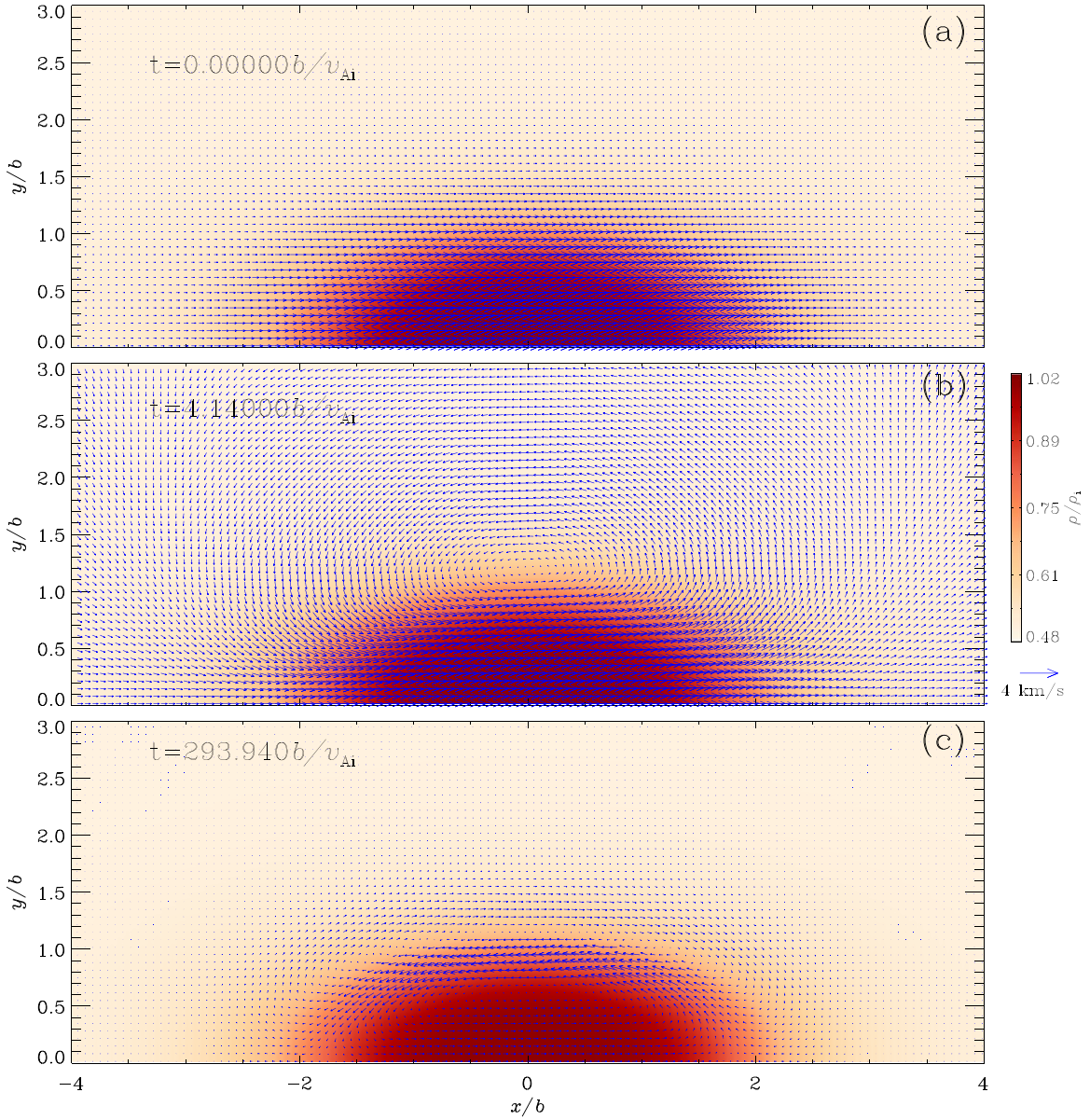
Figure 3. Distributions in the transverse (x–y) plane of the mass density (ρ, filled contours) and the velocity field (arrows) at the loop apex ($z = L/2$) at a selected number of times as labeled. Examined here is a loop that experiences kink oscillations polarized along the major axis, so only one-half of the system is shown. This loop is characterized by an aspect ratio $a/b = 2$ and a density ratio $\rho_i/\rho_e = 2$. The snapshots are taken from the animation attached to this figure. The animated figure runs from $t = 0$ to $724.5\ b/v_{\mathrm{Ai}}$.

(An animation of this figure is available.)

absorption for kink oscillations in loops with circular cross sections (see, e.g., Figure 12 in Goossens et al. 2014).

The same loop system is further examined in Figure 4, where we plot the distributions of the x-component of the fluid velocity in the $x = 0$ plane (Figure 4(a)) and the $z = L/2$ plane (i.e., loop apex, Figure 4(b)) at a time when the system has sufficiently evolved. We also show how the distribution of v_x along the y-direction for $(x, z) = (0, L/2)$ evolves with time in Figure 4(c). This temporal evolution reinforces the interpretation of the damping of the kink oscillation in terms of resonant absorption, given that the attenuation of the oscillations in the loop interior ($y \lesssim 0.5\, b$) takes place in conjunction with the enhancement of v_x around the loop boundary. Furthermore, one sees that the stripes corresponding to the v_x enhancements become increasingly inclined with time. In other words, shorter

and shorter spatial scales develop in the v_x profiles, eventually resulting in multiple ripples as seen in Figure 4(b). This behavior is well known for kink oscillations in loops with circular cross sections and has been customarily interpreted as the phase mixing of the localized Alfvén waves that are resonantly converted from collective kink oscillations (see, e.g., Figure 12 in Howson et al. 2019). What our Figure 4 shows is that the resonant coupling of kink modes to and the subsequent phase mixing of localized Alfvén waves are robust in that they take place for loops with elliptical cross sections as well. It is just that, in our case, the ripples are more elongated in the x-direction, which is understandable given that M-modes are polarized along the major axis. As for Figure 4(a), one sees the concentration of the v_x enhancements at the loop boundary as well. These enhancements tend to increase from the loop
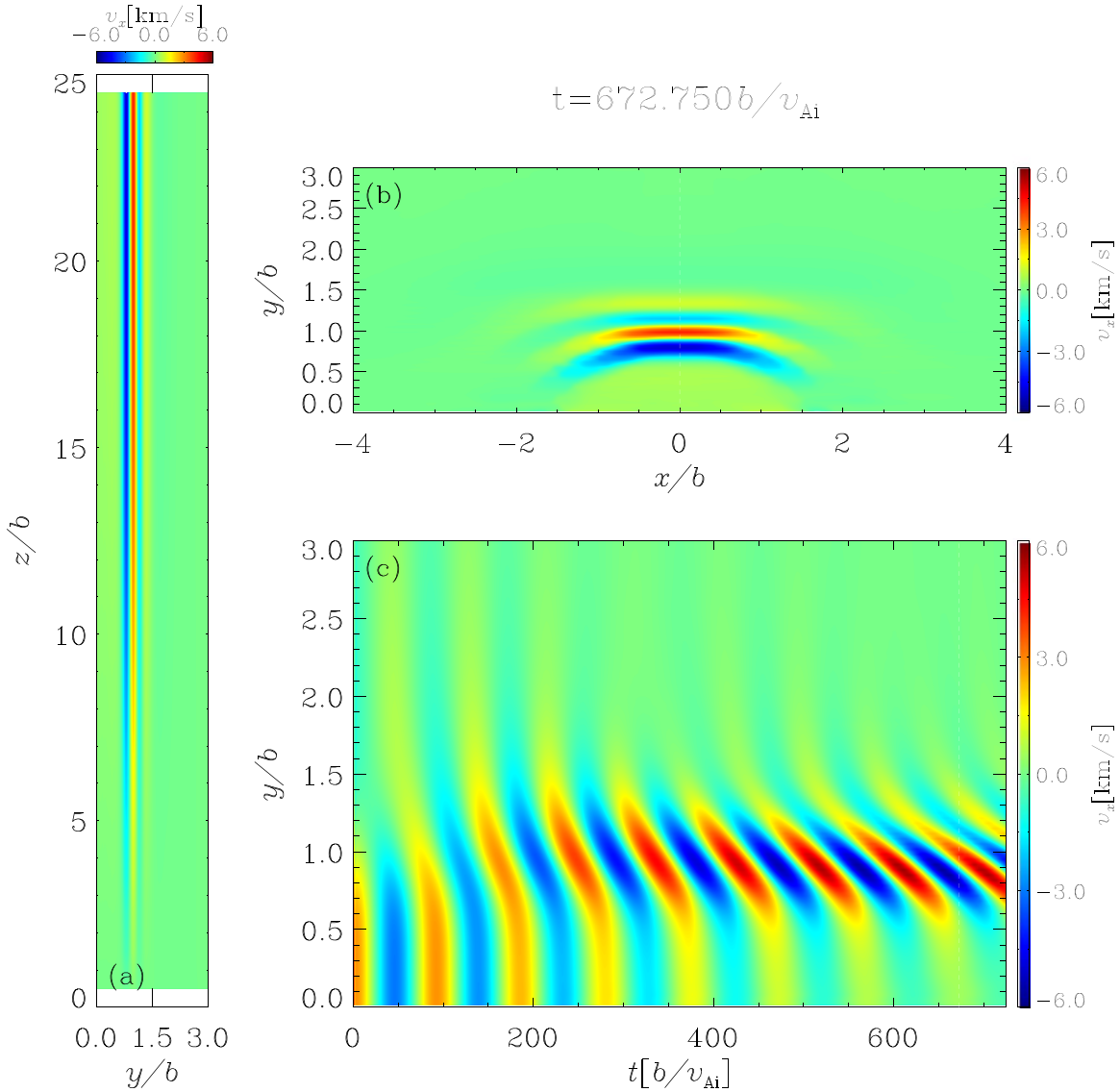
Figure 4. Distributions of the x-component of the fluid velocity (v_x) in (a) the $x = 0$ plane and (b) the $z = L/2$ plane at a time when the system has sufficiently evolved. Shown in (c) is the temporal evolution of the distribution of v_x along the y-direction for $(x, z) = (0, L/2)$. Examined here is a loop that experiences kink oscillations polarized along the major axis. This loop is characterized by an aspect ratio $a/b = 2$ and a density ratio $\rho_i/\rho_e = 2$.

footpoint to loop apex, as expected for fundamental modes. We have performed a more detailed examination on the resonant conversion of the kink oscillations into localized Alfvénic motions. This examination is presented in Appendix B to avoid digressing too much from our discussions on the characteristic timescales of the decaying kink oscillations.

Now move on to the m-modes. Figure 5 overviews, in a form identical to Figure 2, the temporal evolution of the y-component of the fluid velocity at the loop apex ($(x, y, z) = (0, 0, L/2)$). Note that the damping profile ($D(t)$) is now assigned the subscript m and derives directly from the extrema in each series of $v_{y,\mathrm{apex}}$. Note also that the curves and symbols corresponding to $a/b = 1$, namely the cases where we examine loops with circular cross sections, are not replotted from Figure 2 but found with independent simulations. However, these curves and symbols coincide exactly with those in Figure 2, despite the different direction of the initial velocity perturbations and the different numerical grid. This coincidence is reassuring in that for loops with circular cross sections, the

M- and m-modes should be degenerate. As is the case for Figure 2, the impulsive phase can be discerned in Figures 5(a) and (c), characterized by the initial short-duration reductions in the oscillation magnitudes. Interestingly, one sees from the lower row that the magnitudes of the oscillations in the time interval after the impulsive phase tend to decrease with the aspect ratio a/b for a fixed density ratio (see, e.g., the asterisks at $t \approx 40\,b/v_{\mathrm{Ai}}$), in contrast to what happens for the M-modes. This is understandable by invoking also the inertia argument, by which we mean the extent to which a loop is aware of its surrounding fluids. Now the majority of the fluid parcels in the loop interior move along the y-direction, meaning that when a/b increases, the velocity field becomes increasing normal to the areas where the loop fluids get in contact with their surroundings. As a consequence, the ambient medium fluids play an increasingly important role in the loop oscillations, thereby lowering the capability for loops to trap the energy contained in the initial perturbations. In view of the inertia argument, one would expect that the oscillations in the first
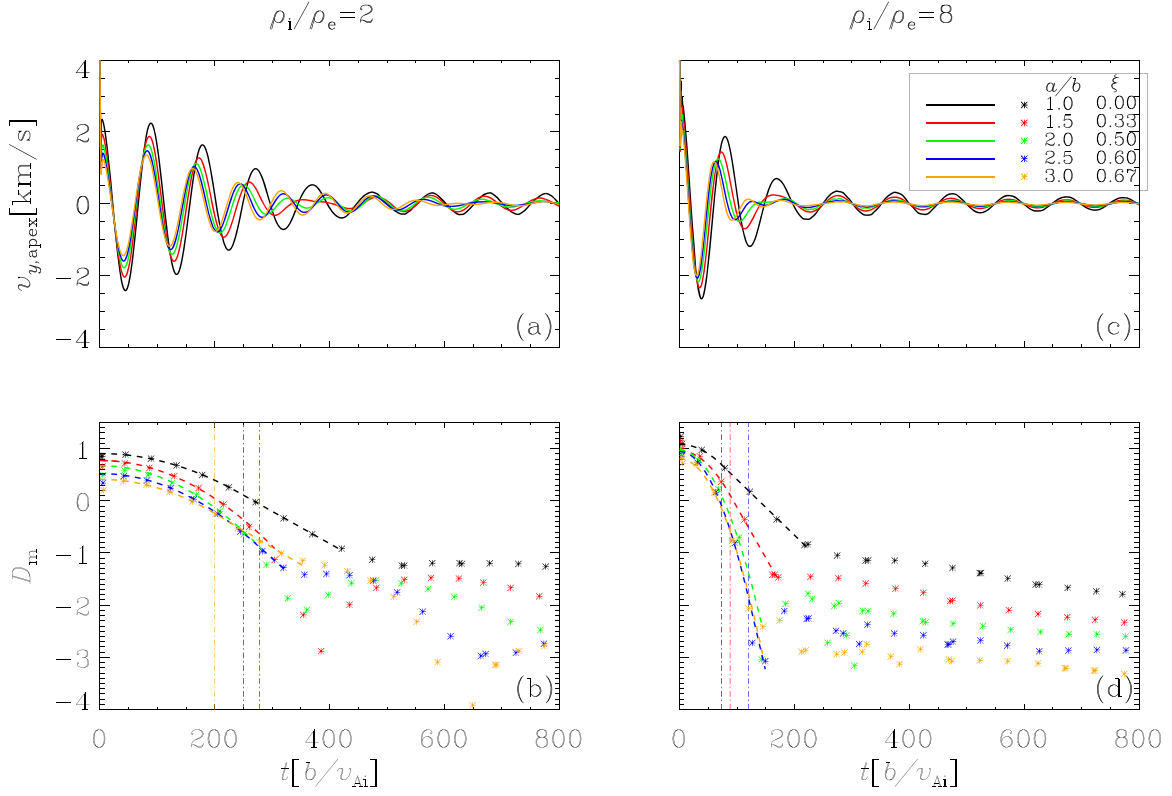
Figure 5. Similar to Figure 2, but for kink oscillations polarized along the minor axis (m-modes), hence the subscripts y in $v_{y,\text{apex}}$ and m in D_{m}.
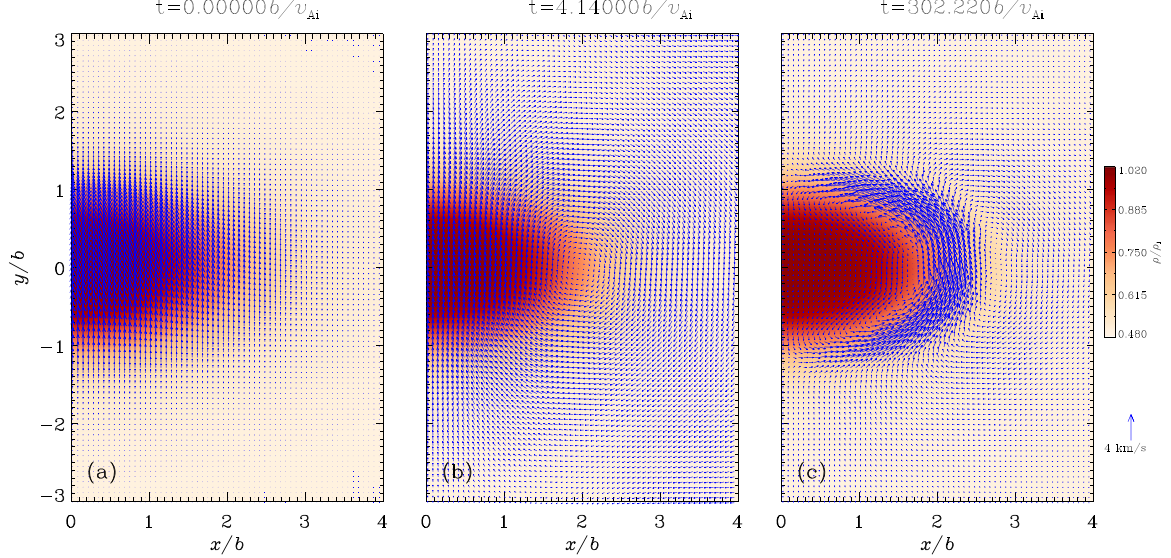

Figure 6. Similar to Figure 3, but for kink oscillations polarized along the minor axis. The animated figure runs from $t = 0$ to 310.5 b/v_{Ai}.
(An animation of this figure is available.)

cycle would strengthen for a larger density ratio, and this is indeed seen if one compares Figures 5(b) and (d).

The m-mode oscillations experience some substantial damping after the impulsive phase. To show what happens during this interval, we have built an animation in the same format as the one attached to Figure 3 for the same loop examined therein. A few representative snapshots are extracted from this animation and presented in Figure 6. In addition, slightly revising the form of Figure 4 to account for the present

polarization, we have also constructed the distributions of v_y in appropriate x–z (Figure 7(a)), x–y (Figure 7(b)), and x–t planes (Figure 7(c)). Similar to the M-modes, one sees the development of the characteristic vortical motions after the impulsive leaky phase (Figure 6(b)), the accumulation of the Alfvén modes at the loop boundary (Figures 6(c)), and the increasing inclination of the velocity enhancement stripes with respect to the t-axis (Figure 7(c)). All these signatures further demonstrate the robustness of the notions of resonant absorption and phase
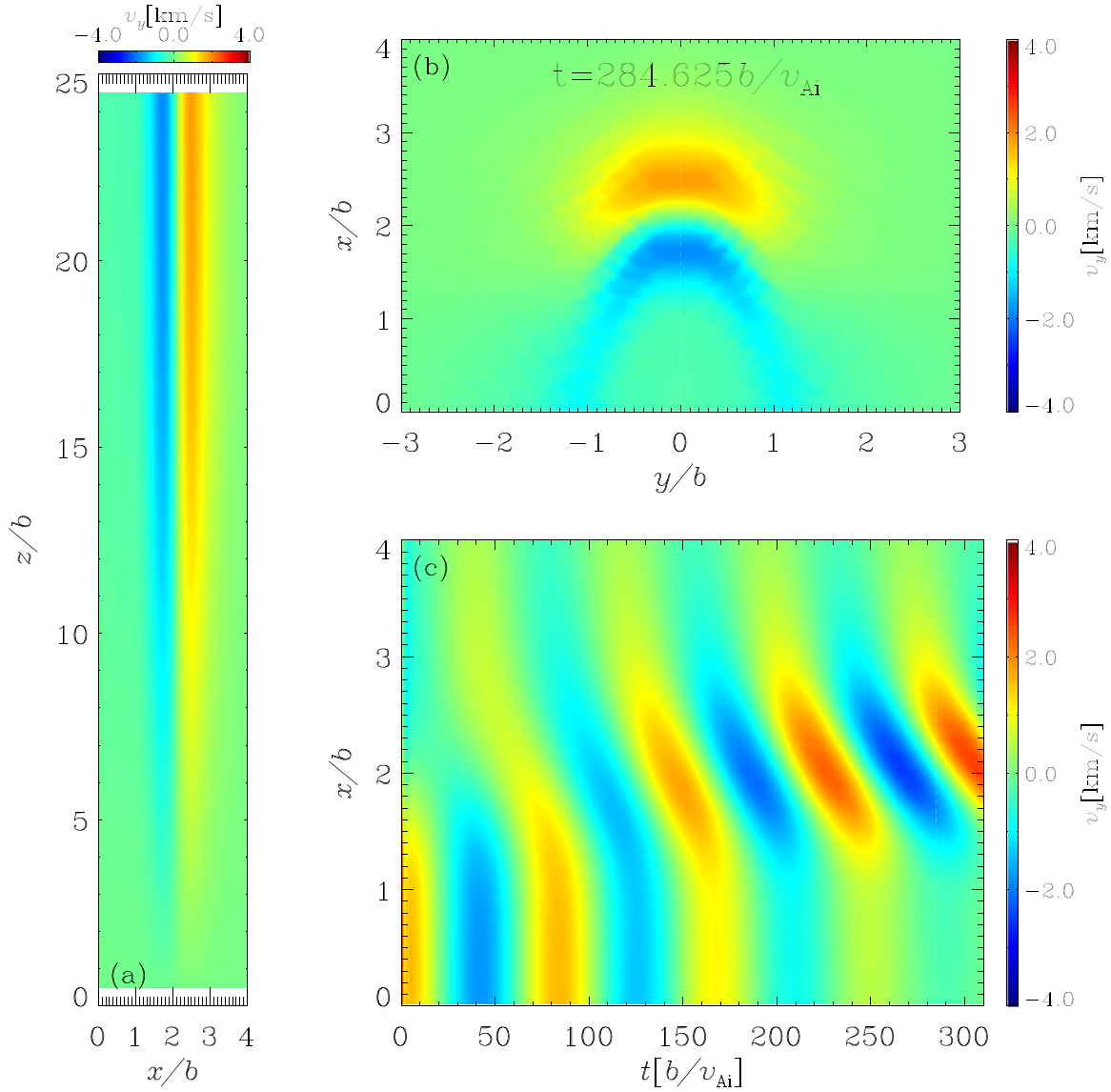
Figure 7. Similar to Figure 4, but for kink oscillations polarized along the minor axis. Presented here are the distributions of v_y in (a) the $y = 0$ plane and (b) the $z = L/2$ plane at a time when the system has sufficiently evolved. Furthermore, given in (c) is the temporal evolution of the x-distribution of v_y for $(y, z) = (0, L/2)$.

mixing, "robust" in the sense that these processes operate for loops with circular and elliptic cross sections alike, and for M- and m-modes alike.

Comparing the lower rows in Figures 2 and 5, one sees that for a given combination $[\rho_i/\rho_e, a/b]$, the m-mode damps more strongly than the corresponding M-mode. Consequently, the irregular large-time behavior appears earlier, and sometimes an exponential envelope can no longer be found in our fitting procedure (see, e.g., the cases with $a/b = 1.5$ and 2 in Figure 5(b)). At this point, one may question the origin of this large-time behavior. From the computational standpoint, one naturally expects that a damping profile will not diminish indefinitely given the necessarily finite grid resolution, even if the profile does approach zero. We have therefore experimented with a finer grid with a resolution two times higher than the base computations for a selected number of m-mode simulations. The large-time oscillations indeed reach a lower level, indicating that they are at least partly of numerical origin. However, we choose not to present the results from the fine-grid computations for two reasons. First, they offer no more

than one additional extreme for us to perform the fitting procedure on. Second, and more importantly, the amplitudes of the oscillations in the large-time behavior are no more than a few percent of the magnitude of the initial perturbation. This makes their observational identification unlikely.

Figure 8 collects the characteristic timescales for the M-modes (circles) and m-modes (diamonds) that we have computed. Given from top to bottom are the periods (P), the damping times in the Gaussian stage (τ^G), and those in the exponential stage (τ^E). The two density ratios ($\rho_i/\rho_e = 2$ and 8) are shown with different colors. Note that here the timescales are in units of the transverse Alfvén time (b/v_{Ai}), and simply dividing them by $L/b = 50$ yields the values in units of the longitudinal one (L/v_{Ai}). Let us recall that the periods are derived by doubling the average temporal spacing between two adjacent extrema for any combination $[\rho_i/\rho_e, a/b]$ in the interval where the fitting procedure is allowed. Let us further recall that the damping times are derived from the fitting procedure. For the M-modes (m-modes), the symbols are connected by the solid (dashed) curves unless the symbols are
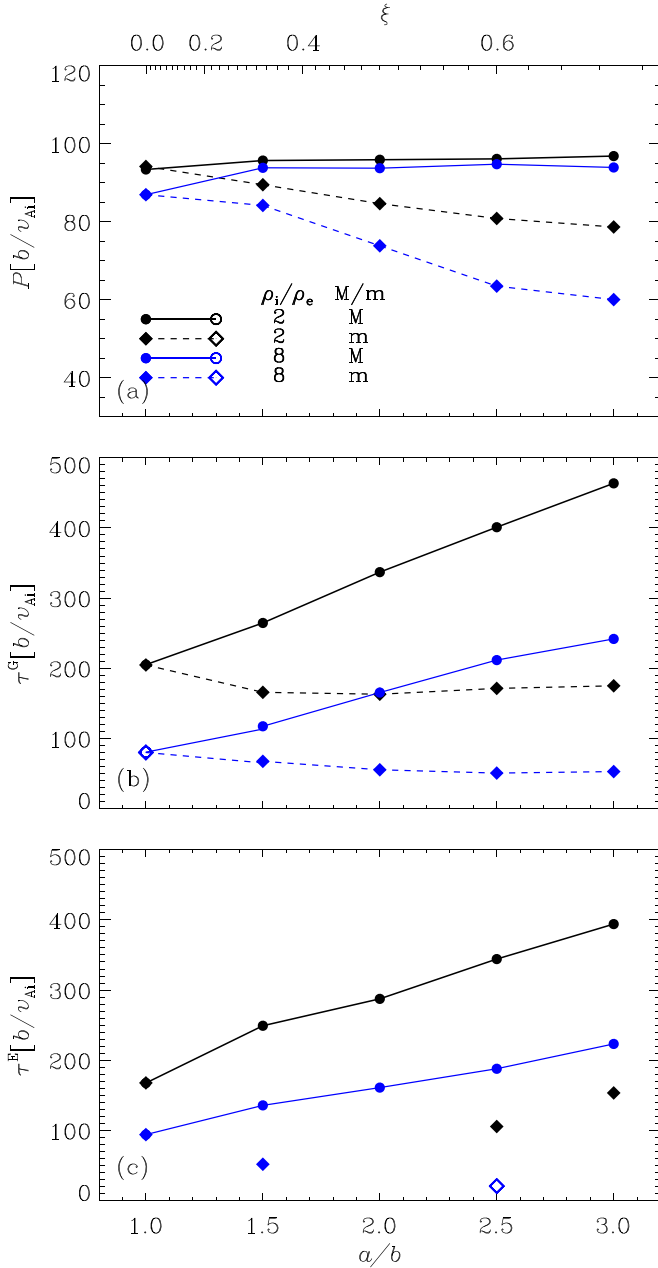
10

Figure 8. Dependence on the aspect ratio (a/b) of (a) the periods (P) and (b), (c) damping times (τ^G, τ^E) of the kink oscillations supported by loops with elliptic cross sections and transverse profiles described by Equation (2). Two different density ratios are examined as labeled by the different colors. The symbols represent the values found via best fitting our numerical results, and the open symbols represent the values that are not as reliable as the solid symbols. The circles (diamonds) correspond to the M-modes (m-modes), namely the modes polarized along the major (minor) axis. When not too sparse, the symbols are connected by the solid and dashed curves, respectively. The flattening $\xi = 1 - b/a$ labeled here represents the deviation of a cross section from a circular one.

too sparse. This happens for the m-modes because one sees only a limited number of diamonds in Figure 8(c), which in turn arises from the absence of an exponential stage. A small number of the symbols are open, which is intended to suggest that these values may not be as reliable as those represented by the solid symbols (see, e.g., the open diamond corresponding to $a/b = 1$ in Figure 8(b)). We adopt the following criteria to judge whether a damping time is reliable, which comes

primarily from the consideration of the degree of freedom involved in the fitting process. Note that while the fitting model (Equation (6)) nominally involves three independent parameters, only two (A^G and τ^G) are relevant when an exponential stage is absent. We therefore deem the fitting procedure to be inapplicable altogether if there are no more than five (four) extrema that can be fitted when an exponential stage does (does not) exist. However, this does not really happen. What happens is that when both stages are present, sometimes there is only one extreme in either the Gaussian or the exponential stage. The former situation arises for the m-mode and equivalently the M-mode computations with $a/b = 1$ for $\rho_i/\rho_e = 8$. The latter happens for our computation of the m-mode with $a/b = 2.5$ and $\rho_i/\rho_e = 8$. Both situations can be found in Figure 5(d). We consider the values derived in such cases to be not that reliable.

Let us examine the periods first, shown in Figure 8(a). For loops with circular cross sections (aspect ratio $a/b = 1$), one sees the expected behavior that the M- and m-modes are degenerate, and their periods tend to decrease with the density ratio ρ_i/ρ_e. This is well known for loops with step (e.g., Edwin & Roberts 1983) and steep transverse profiles (e.g., Goossens et al. 2008). In the TT limit, the period in both cases reads as

$$P = \frac{\sqrt{2}L}{v_{Ai}} \sqrt{1 + \frac{\rho_e}{\rho_i}}. \tag{7}$$

One further sees that for a given density ratio, the periods of the M-modes (m-modes) increase (decrease) with the aspect ratio. The same qualitative dependence is seen in the analytical study by R03, despite the TTTB approximation and the different transverse profiles adopted therein. In the zero-β calculations, R03 worked out the extreme case with $a/b \rightarrow \infty$, and Equation (59) therein shows that P_M and P_m become $2L/v_{Ai}$ and $2L/v_{Ae}$, respectively. In other words, in the case of infinitely elongated cross sections, P_M does not involve the ambient corona at all, whereas P_m is entirely determined by the ambient corona. R03 invoked the inertia argument to explain this extreme behavior; namely, the polarization of the M-modes (m-modes) means that the elastic interaction between the loops and their surroundings vanishes (maximizes). As has been discussed for Figures 2 and 5, the same line of thinking applies to the interpretation of the a/b dependence of the oscillation magnitude right after the impulsive leaky phase as well. Provided this reasoning is valid, one may expect the following features in Figure 8, where the periods are measured in units of b/v_{Ai}. For a given ρ_i/ρ_e, with a/b increasing, both P_M and P_m should eventually show little dependence on a/b. Furthermore, at sufficiently large a/b, one expects that P_M shows little dependence on ρ_i/ρ_e, whereas P_m will decrease monotonically with ρ_i/ρ_e. Both of these features are indeed seen in our numerical results. Combining these features and what happens for $a/b = 1$, one can then readily understand the overall behavior for the departure of P_M from P_m being stronger for large a/b and large ρ_i/ρ_e.

Now move on to the damping times as shown in Figures 8(b) and (c). For loops with circular cross sections, Pascoe et al. (2016c) proposed that

$$\frac{\tau^G}{P} = \frac{2}{\pi\kappa\epsilon^{1/2}}, \quad \frac{\tau^E}{P} = \frac{4}{\pi^2\kappa\epsilon}, \tag{8}$$

valid in the TTTB limit and for transverse profiles characterized by a transition layer (TL) linearly connecting a uniform interior

to a uniform ambient medium. Here by "linearly" we mean that the mass density depends on the transverse coordinate in a linear fashion. And by "TB" we mean that $\epsilon \equiv l/R \ll 1$, where l is the layer width and R is the mean loop radius. Note that P in this case is given by Equation (7), and κ is determined by the density ratio as

$$\kappa = \frac{\rho_i/\rho_e - 1}{\rho_i/\rho_e + 1}. \tag{9}$$

Equation (8) suggests that both τ^G and τ^E decrease with ρ_i/ρ_e. This qualitative behavior is also seen in our numerical results. Furthermore, Figures 8(b) and (c) indicate that the same trend applies to both M- and m-modes at a given a/b. For a given ρ_i/ρ_e, on the other hand, Figure 8(b) suggests that τ_M^G increases with a/b, whereas the opposite happens for τ_m^G. It is just that τ_M^G possesses a stronger a/b dependence than τ_m^G does. The end result is that, for sufficiently large a/b, the difference between τ_M^G and τ_m^G is significant for both density ratios. One further sees from Figure 8(c) that τ_M^E increases with a/b for a given ρ_i/ρ_e. However, the dependence of τ_m^E on a/b does not seem to be monotonic. While the limited number of diamonds does not permit us to draw a firm conclusion on this, it seems nonetheless safe to say that τ_M^E is longer than τ_m^E for both density ratios. Note that when using the analytical expressions given by R03, we have deduced that $\tau_M^E < \tau_m^E$ for $\rho_i/\rho_e \lesssim 5$ but $\tau_M^E \gtrsim \tau_m^E$ when $\rho_i/\rho_e \gtrsim 5$. The former behavior is not seen in Figure 8(c), though the latter is. This difference from the R03 results may result from the difference in the adopted transverse profiles or the questionable applicability of the TB approximation given our value of α. Whatever the source is, this discrepancy strengthens the importance of examining different profile choices or moving away from the TB approximation, as far as the properties of kink oscillations in loops with elliptic cross sections are concerned.

4. Discussion

So what seismological applications do we expect, given our computations for kink oscillations in coronal loops with elliptic cross sections? Let us start by noting that aspect ratios (a/b) of 2 or larger are compatible with recent spectroscopic measurements (Kucera et al. 2019). Furthermore, observational surveys indicate that the majority of decaying kink oscillations are associated with eruptive events in the lower corona (e.g., Zimovets & Nakariakov 2015; Nechaeva et al. 2019). As such, the initial transverse perturbations that impact on a loop are unlikely to prefer the direction of one axis of the elliptical cross section to the direction of the other. Adopting the customary assumption that linear theories apply, one then expects that the initial perturbations can be decomposed into two independent components, one along the major and the other along the minor axis. Consequently, the M- and m-modes can be excited simultaneously. On the other hand, it is unlikely that the line of sight of an instrument is always aligned with a particular axis. It is therefore possible for both imagers and spectrographs to sample kink oscillations that are actually a superposition of M- and m-modes.

Our numerical results suggest the following seismological scheme, which is feasible at least in principle. For simplicity,

let us focus on fundamental kink oscillations and consider only the application of the periods (P) and damping times (τ). Let us further assume that the plasma β for typical active-region loops is too small to be relevant, and likewise, the loops are long enough for the thin-tube approximation to apply. It follows from straightforward dimensional analysis that P and τ can be formally formulated as

$$P_M = \frac{L}{v_{Ai}} \mathcal{P}_M(\rho_i/\rho_e, a/b, \alpha), \tag{10}$$

$$P_m = \frac{L}{v_{Ai}} \mathcal{P}_m(\rho_i/\rho_e, a/b, \alpha), \tag{11}$$

$$\tau_M^G = \frac{L}{v_{Ai}} \mathcal{G}_M(\rho_i/\rho_e, a/b, \alpha), \tag{12}$$

$$\tau_m^G = \frac{L}{v_{Ai}} \mathcal{G}_m(\rho_i/\rho_e, a/b, \alpha), \tag{13}$$

$$\tau_M^E = \frac{L}{v_{Ai}} \mathcal{E}_M(\rho_i/\rho_e, a/b, \alpha), \tag{14}$$

$$\tau_m^E = \frac{L}{v_{Ai}} \mathcal{E}_m(\rho_i/\rho_e, a/b, \alpha). \tag{15}$$

Evidently, the specific forms of the functions $\mathcal{P}$, $\mathcal{G}$, and $\mathcal{E}$ depend on the specific form of the transverse density profile. While the symbol α is used, it is intended to represent some dimensionless steepness parameter that characterizes the spatial scale of the transverse density distribution (say, the ratio of this spatial scale to the half minor axis). In other words, it does not have to have the same meaning as in Equation (2). For the profile linear in some elliptic coordinate, R03 has offered explicit forms for $\mathcal{P}_M$, $\mathcal{P}_m$, $\mathcal{E}_M$, and $\mathcal{E}_m$. These expressions are applicable provided that the steepness parameter ensures the thin-boundary approximation. On the other hand, our computations demonstrate that the functions in Equations (10)–(15) can be numerically established for the majority of the equilibrium parameters of interest. Regardless, the point is that the wave quantities involve only four equilibrium parameters, namely, the longitudinal Alfvén time (L/v_{Ai}), the density ratio (ρ_i/ρ_e), the aspect ratio (a/b), and the steepness parameter α. It therefore follows that these four parameters can be inverted for, provided that the M- and m-modes can be adequately separated. From the perspective of practical implementation, Figure 8(a) indicates that it is preferable that both the density ratios and the aspect ratios are significant. However, in principle, the seismological inversion is not limited to such cases, given the enhanced spectral resolution offered by modern time-frequency analysis methods (e.g., Wang et al. 2018).

Is there any indication that the M- and m-modes may have been observed? For simplicity, let us focus only on the periods and insist that only fundamental modes are involved in the observed signals. We are then inspired to look for multiperiodic signals comprising periodicities that are different but remain of the order of the longitudinal Alfvén time. Such instances have indeed been observed since the early measurements with TRACE (e.g., Verwichte et al. 2004; Guo et al. 2015; Pascoe et al. 2016a; Duckenfield et al. 2019; see also the review by Andries et al. 2009, and references therein). However, nearly all of these observations are spatially resolved, enabling the measurement of the axial

distributions of the phases of the component signals. In general, it was found that the component signal with a long period (P_{long}) possesses a different phase profile from the component with a short period (P_{short}). This fact, together with the fact that P_{long} is not far from $2P_{\mathrm{short}}$, is therefore more in line with the interpretation of the signals as comprising a fundamental mode and its axial harmonic. Under the assumption that coronal loops possess circular cross sections, this has inspired a series of studies that exploit the period ratio ($P_{\mathrm{long}}/P_{\mathrm{short}}$) to seismologically deduce such equilibrium parameters as the axial density scale height (e.g., Andries et al. 2005) and the axial magnetic field scale height (e.g., Verth & Erdélyi 2008). Having said that, we note one exception found in the multiperiodic signal associated with path C in a loop arcade imaged with TRACE as reported by Verwichte et al. (2004, hereafter V04). In this case, two different periods were identified, the shorter one being $P_{\mathrm{short}} \approx 315 \pm 144$ s and the longer one being $P_{\mathrm{long}} \approx 405 \pm 35$ s (Table 2 in V04). Two sets of values are given there, one from a wavelet analysis and the other from a curve-fitting procedure. We prefer the latter, because it also yields the damping times for both periodicities. Interestingly, V04 noted that a Gaussian-like damping is more appropriate for both periodicities than an exponential damping. The derived damping times are $\tau_{\mathrm{short}} = 920 \pm 290$ s and $\tau_{\mathrm{long}} = 1550 \pm 640$ s for the short- and long-period components, respectively. While the amplitude of the long-period signal was found with statistical significance to decrease away from the loop apex as expected for fundamental modes, there was only limited indication for the short-period signal to show the same behavior. Nonetheless, let us assume that this P_{long} belongs to the M-mode and attribute P_{short} to the m-mode, with both modes being axial fundamentals. From Figure 8(a) we see that P_{M} is sensitive to neither a/b nor $\rho_{\mathrm{i}}/\rho_{\mathrm{e}}$ when $a/b \gtrsim 1.5$. Dividing the numbers in V04 by a scaling parameter of ~ 4.3[3] and placing the resulting values in Figure 8(a), one can see that a combination of [a/b, $\rho_{\mathrm{i}}/\rho_{\mathrm{e}}$] = [2.5, 2] can readily account for the observations. While admittedly not a proper inversion, this comparison nonetheless shows that the particular measurements associated with a particular loop in V04 are not incompatible with interpretation in terms of fundamental M- and m-modes in loops with elliptic cross sections.

Let us accept that decaying kink oscillations are excited by coronal eruptive events. One then expects that the time series of, say, transverse loop displacements involving at least two periodicities should be rather common to see if the cross sections of coronal loops are more likely to be elliptic, or noncircular to be precise. This does not seem to be the case, for multiperiodic signals seem to be present in only a small fraction of available measurements of kink oscillations. On top of that, these multiperiodic signals tend to agree more with the understanding in terms of the existence of axial harmonics. So why does this "scarcity of multiperiodic oscillations" happen? There are certainly many possible reasons, and we offer but two. It may be that when initially displacing coronal loops, the impulsive drivers prefer one half-axis to the other for some unknown reason. Alternatively, it may be that the cross sections of oscillating loops are not far from a circular one.

Discussing the second possibility further, we note that oscillating loops are only a subset of coronal loops, which in turn occupy only a subset of magnetic flux tubes (e.g., Schrijver et al. 2010; Malanushenko & Schrijver 2013). Regarding the cross-sectional properties, if oscillating loops are not representative of coronal loops, then one natural question arises as to why only those loops with nearly circular cross sections tend to be displaced. If, on the other hand, oscillating loops are representative of coronal loops, then one naturally questions why the density enhancements tend to fill a certain set of magnetic flux tubes in such a manner as to make the cross sections nearly circular. As pointed out by Malanushenko & Schrijver (2013), if indeed there, then this last selection effect actually places some rather stringent constraints on the mechanisms heating the quiescent corona. It is highly nontrivial to address any of the above-mentioned issues, given the inevitable need to measure the coronal magnetic field.

The seismological applications of Equations (10)–(15) have been discussed for the ideal situation that both M- and m-modes can be discerned, and that the Gaussian and exponential damping envelopes can be differentiated. We argue that the "scarcity of multiperiodic oscillations" does not mean that these equations cannot be further exploited, for which we offer only two possibilities. First, it seems necessary to further exploit the catalogs of kink oscillations compiled in Zimovets & Nakariakov (2015) and Nechaeva et al. (2019) to look for more multiperiodic signals with advanced time-frequency analysis methods. Provided that the ideal situation indeed arises, one ends up with an inversion problem that is likely to be overdetermined; namely, more observables appear than the equilibrium parameters to invert for. Second, it is possible to constrain the equilibrium parameters with the available measurements even if there is only one periodicity. Suppose that this periodicity belongs to an M-mode, and that a Gaussian envelope can be distinguished from an exponential one. In this case, Equations (10), (12), and (14) enable the construction of an inversion curve in the four-dimensional parameter space spanned by L/v_{Ai}, $\rho_{\mathrm{i}}/\rho_{\mathrm{e}}$, a/b, and α. While this underdetermined inversion seems less than ideal, it reaches the same status as what one can do when only P and τ^{E} are exploited for kink oscillations in loops with circular cross sections (e.g., Arregui et al. 2007; Goossens et al. 2008; Soler et al. 2014). Whatever the possible uncertainties in a/b, this nonetheless offers an independent means of offering the important information about the geometrical properties of the cross sections of coronal loops.

5. Summary and Concluding Remarks

This research was motivated by the apparent lack of a detailed study, from the initial-value-problem perspective, on the decaying kink oscillations in coronal loops with elliptic cross sections. A noncircular cross section, however, has been suggested on both theoretical and observational grounds. We approached this problem by numerically following the responses of straight loops with elliptic cross sections to initial transverse velocity perturbations. We adopted sufficiently weak initial perturbations to focus on kink oscillations in the linear regime. In addition, inspired by the relevant eigenmode analysis by Ruderman (2003, R03), we applied two independent sets of initial perturbations, thereby exciting kink oscillations with two independent polarizations. Based on the

---

[3] For $a/b \gtrsim 1.5$, one sees that $P_{\mathrm{M}} \sim 95b/v_{\mathrm{Ai}} = 1.9L/v_{\mathrm{Ai}}$. Attributing $P_{\mathrm{long}} \approx 405$ s as measured by V04 to this P_{M}, we find that the measured periods and damping times need to be scaled by a factor of $405/95 \sim 4.3$ for these values to be placed in Figure 8. This is not to say that path C in V04 is required to possess an L/b of 50 or a b/v_{Ai} of 4.3 s. Rather, what we assume is that the longitudinal Alfvén time L/v_{Ai} attains $405/1.9 \approx 213$ s, given that P_{M} is expected to be independent of L/b when L/b is sufficiently large.

pertinent velocity fields, we used M- and m-modes to denote the oscillations that are primarily polarized along the major and minor axes, respectively. For both polarizations, we performed a rather comprehensive study on how the mode properties depend on the major-to-minor-half-axis ratio a/b. Two internal-to-external density ratios ($\rho_i/\rho_e = 2$ and 8) were adopted to represent the low- and high-density ratio situations. Two different specifications of the transverse profiles were also examined. One was given by Equation (2), and the pertinent results are presented in the text. The other was identical to what was adopted by R03 (see Equation (A3)), and the pertinent results are presented in the appendix for validation purposes.

Common to both transverse profiles, and common to both density ratios, we find that the temporal evolution of the transverse displacements is in general characterized by a damping profile that comprises a Gaussian envelope and an exponential one. In addition, this attenuation of the collective motion is accompanied by the enhancement of the transverse Alfvénic motions in an area surrounding the loop boundary, where small transverse spatial scales develop with time. In other words, our results lend further support to the robustness of the resonant coupling of the kink modes to and the consequent phase mixing of localized Alfvénic motions, despite an elliptic rather than a circular loop cross section. For all computations we conducted, we find that the periods of the M-modes (P_M) increase with a/b for a given ρ_i/ρ_e, whereas the opposite takes place for the periods of the m-modes (P_m). When the aspect ratio a/b is fixed, both P_M and P_m tend to decrease with the density ratio. During the Gaussian stage, the characteristic damping time for the M-modes τ_M^G tends to be longer than that for the m-modes τ_m^G. This makes it difficult to find a proper exponential damping envelope in some m-mode computations. For the cases where an exponential envelope exists, the damping time for the m-mode τ_m^E may be longer than its M-mode counterpart τ_M^E for the profile examined by R03 for the low density ratio, even though $\tau_m^E < \tau_M^E$ in most cases.

We discussed the potential applications of our numerical findings in the context of coronal seismology, assuming that loops are sufficiently long and the plasma β is sufficiently small. In particular, we showed that one oscillating loop in a loop arcade imaged with TRACE and reported by Verwichte et al. (2004) is likely to host simultaneously an M-mode and an m-mode. As such, some information regarding the aspect ratio of the cross section of the oscillating loop can be deduced. We showed that the inversion problem may be overdetermined in the ideal case where an M-mode and an m-mode are simultaneously measured, and an exponential damping envelope can be distinguished from a Gaussian one. In this case, the number of measureables (P_M, P_m, τ_M^G, τ_m^G, τ_M^E, and τ_m^E) exceeds the number of the equilibrium parameters to invert for (L/v_{Ai}, ρ_i/ρ_e, a/b, and α). Here, L/v_{Ai} represents the longitudinal Alfvén time, and α represents some dimensionless steepness parameter characterizing the spatial scale of the transverse inhomogeneity. It was further shown that some information on a/b can still be gathered even in the underdetermined cases where only one periodicity can be found, provided that both damping envelopes can be measured.

Having said that, we stress that this study is only one of the first steps toward addressing kink oscillations in realistic coronal loops. For instance, we assumed that the equilibrium parameters are homogeneous in the axial direction, meaning that we cannot address the influence on the kink mode

properties of such effects as the axial density stratification (e.g., Andries et al. 2005; Dymova & Ruderman 2006) or loop expansion (e.g., Howson et al. 2019, and references therein). Likewise, neglecting the loop curvature means that we cannot address the importance relative to resonant absorption of, say, lateral leakage for damping kink oscillations (Terradas et al. 2006a; McLaughlin & Ofman 2008; Selwa et al. 2011a). Finally, we chose to examine only the linear regime to initiate our studies on kink oscillations in loops with elliptic cross sections. For stronger oscillations, the velocity shear associated with both the kink mode itself and the phase-mixed Alfvénic motions is known to be more prone to the Kelvin–Helmholtz instability (e.g., Heyvaerts & Priest 1983; Browning & Priest 1984; Antolin et al. 2015; Magyar & Van Doorsselaere 2016; Guo et al. 2019b; Hillier et al. 2019). It will be informative to examine what happens if we replace the circular cross sections in this extensive series of studies with an elliptic one.

Appendix A
Kink Oscillations in Coronal Loops with Elliptic Cross Sections: A Validation Study

While the numerical implementation of both our equilibrium setup and solution procedure seems rather straightforward (Section 2), it remains reassuring if this implementation can be validated against available analytical results. However, no theories exist to our knowledge that pertain to a transverse profile realized through Equation (2). In fact, the only analytical study that addresses the resonant absorption of kink oscillations in coronal loops with elliptic cross sections seems to be the one by Ruderman (2003, hereafter R03). This section is therefore intended to replace the function $f(x, y)$ with the one examined by R03 and see whether the theoretical expectations therein can be reproduced.

Before proceeding, it is necessary to recall the assumptions made by R03 and the main results therein. Basically, R03 employed zero-β MHD throughout and adopted the thin-tube-thin-boundary (TTTB) approximation. Furthermore, R03 worked in an elliptic coordinate system (s, φ) in the transverse plane (x, y),

$$x = \sigma \cosh s \cos \varphi, \quad y = \sigma \sinh s \sin \varphi, \tag{A1}$$

where s ranges from 0 to ∞ and φ varies between $-\pi$ and π. Any contour of the coordinate s is an ellipse, and R03 chose some s_0 to denote the outer loop boundary beyond which the medium is homogeneous. Letting a and b denote the major and minor half-axes associated with this boundary ($a > b$), one finds that σ and s_0 are then determined through

$$\sigma = \sqrt{a^2 - b^2}, \quad s_0 = \ln \frac{a + b}{\sqrt{a^2 - b^2}}. \tag{A2}$$

The TT approximation translates to $a/L \ll 1$ where L is the loop length. R03 then assumed that the density varies in a form

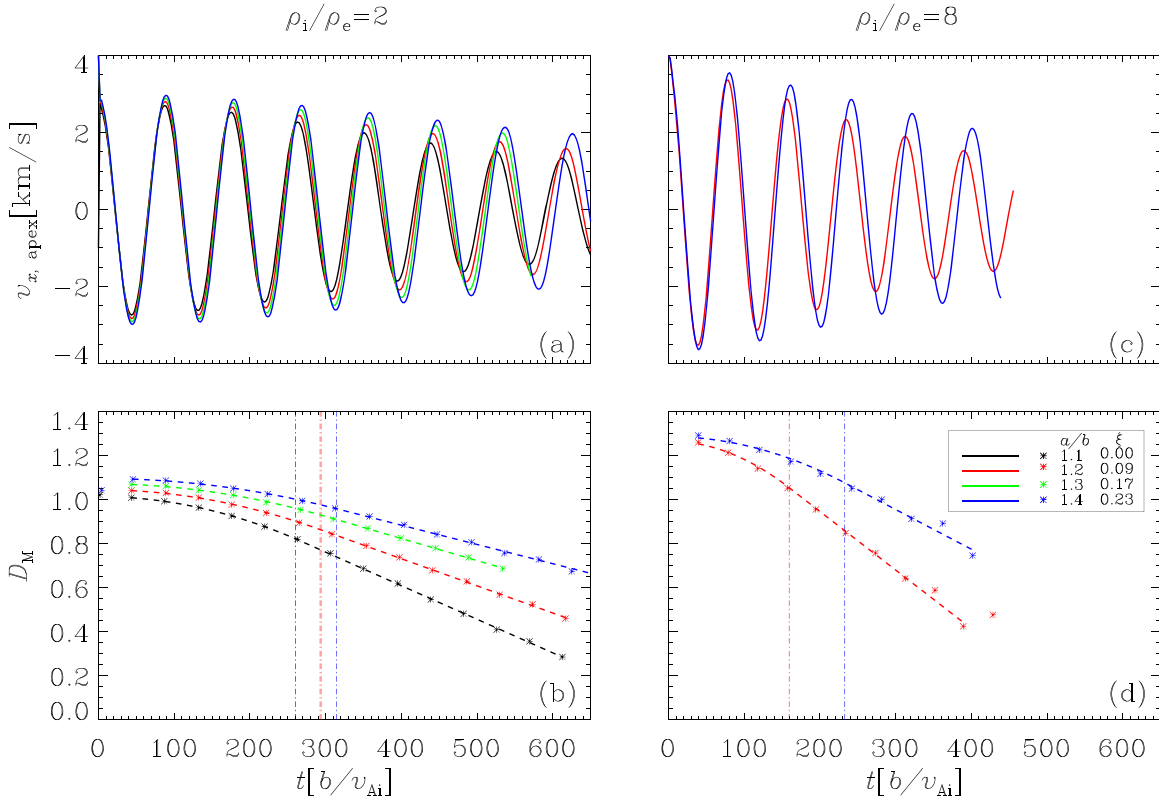**Figure 9.** Temporal evolution of the x-component of the velocity at the loop apex ($v_{x,\mathrm{apex}}$) for kink oscillations polarized along the major axis (M-modes) supported by loops with elliptic cross sections and linear transverse profiles described by Equation (A3). Two density ratios (ρ_i/ρ_e) are adopted, one being 2 (left column) and the other being 8 (right column). A number of aspect ratios (a/b) are examined, as labeled by the different colors. In addition to the time series for $v_{x,\mathrm{apex}}$ itself (upper row), we also extract the extrema therein and plot the natural logarithms of their absolute values (D_{M}) in the lower row. The dashed curves represent the best fit to this discrete series with the three-parameter model given in Equation (6), where a Gaussian damping envelope is distinguished from an exponential one. The switch time from one envelope to the other is represented by the vertical dashed–dotted lines. For validation purposes, the parameter δ/s_0 rather than δ itself is fixed (see the appendix text for details). The flattening $\xi = 1 - b/a$ labeled here represents the deviation of a cross section from a circular one.

identical to Equation (1), with $f(x, y)$ now reading as

$$f(x, y) \equiv f(s) = \begin{cases} 1, & s < s_0 - \delta, \\ (s_0 - s)/\delta, & s_0 - \delta \leqslant s \leqslant s_0, \\ 0, & s > s_0. \end{cases} \quad \text{(A3)}$$

Here, a transition layer (TL) is sandwiched between a uniform interior and a uniform ambient medium. In the elliptic coordinate system, the width of this TL is δ in the s-direction, regardless of φ. However, when translated to a Cartesian coordinate system, the width varies from $b\delta$ in the x-direction to $a\delta$ in the y-direction. By TB, R03 means that $\delta/s_0 \ll 1$.

The following results were then obtained by R03. Focusing on fundamental modes, namely the kink modes with an axial wavenumber $k = \pi/L$, Equation (60) in R03 leads to the periods (P) being given by

$$P_{\mathrm{M}} = \frac{2L}{v_{\mathrm{Ai}}} \sqrt{\frac{\zeta \rho_{\mathrm{ie}} + 1}{\rho_{\mathrm{ie}}(\zeta + 1)}}, \quad P_{\mathrm{m}} = \frac{2L}{v_{\mathrm{Ai}}} \sqrt{\frac{\rho_{\mathrm{ie}} + \zeta}{\rho_{\mathrm{ie}}(\zeta + 1)}}. \quad \text{(A4)}$$

Here, v_{Ai} is the Alfvén speed at the loop axis, and we have used the shorthand notations ζ and ρ_{ie} to represent the aspect ratio a/b and density ratio ρ_i/ρ_e, respectively. In addition, the subscripts M and m correspond to the M- and m-modes, namely the modes polarized along the major and minor axes, respectively. For both modes, we obtain the damping times (τ)

by plugging Equations (84) and (85) into (78) and (79) in R03:

$$\tau_{\mathrm{M}} = \left(1 + \frac{1}{\zeta}\right)^2 \frac{\zeta\rho_{\mathrm{ie}} + 1}{\rho_{\mathrm{ie}} - 1} \frac{P_{\mathrm{M}}}{\pi^2 \delta},$$
$$\tau_{\mathrm{m}} = (1 + \zeta)^2 \frac{\rho_{\mathrm{ie}} + \zeta}{\zeta(\rho_{\mathrm{ie}} - 1)} \frac{P_{\mathrm{m}}}{\pi^2 \delta}. \quad \text{(A5)}$$

Now the question is whether the analytical results from the eigenmode analysis in R03 can be reproduced by time-dependent 3D MHD simulations. Numerically speaking, almost everything, be it the setup of the numerical grid system or the way of exciting kink oscillations, can be inherited from Section 2. It is just that $f(x, y)$ in Equation (2) needs to be replaced with Equation (A3). Consequently, the steepness parameter α therein is now replaced with δ. As in the main text, we fix b to be 1000 km, but allow a/b to vary. However, one sees from Equation (A2) that s_0 decreases with increasing a/b. This means that when some δ is given, $\delta/s_0 \ll 1$ is not necessarily guaranteed. Take $\delta = 0.2$ for instance. For an a/b of 1.04, one finds that $s_0 = 1.97$, and δ/s_0 indeed satisfies the nominal criteria (say, $\delta/s_0 \leqslant 0.1$) for δ/s_0 to be considered small. However, if one takes $a/b = 1.5$, then $s_0 = 0.81$ and hence δ/s_0 attains 0.25, a value that is no longer much smaller than unity. Therefore, in practice, we fix δ/s_0 to be 0.1 for validation purposes while varying a/b between 1.1 and 1.4. Note that we avoid the limit $a/b = 1$ because of the appearance of $\sqrt{a^2 - b^2}$ in Equation (A2). On the other hand, s_0 decreases
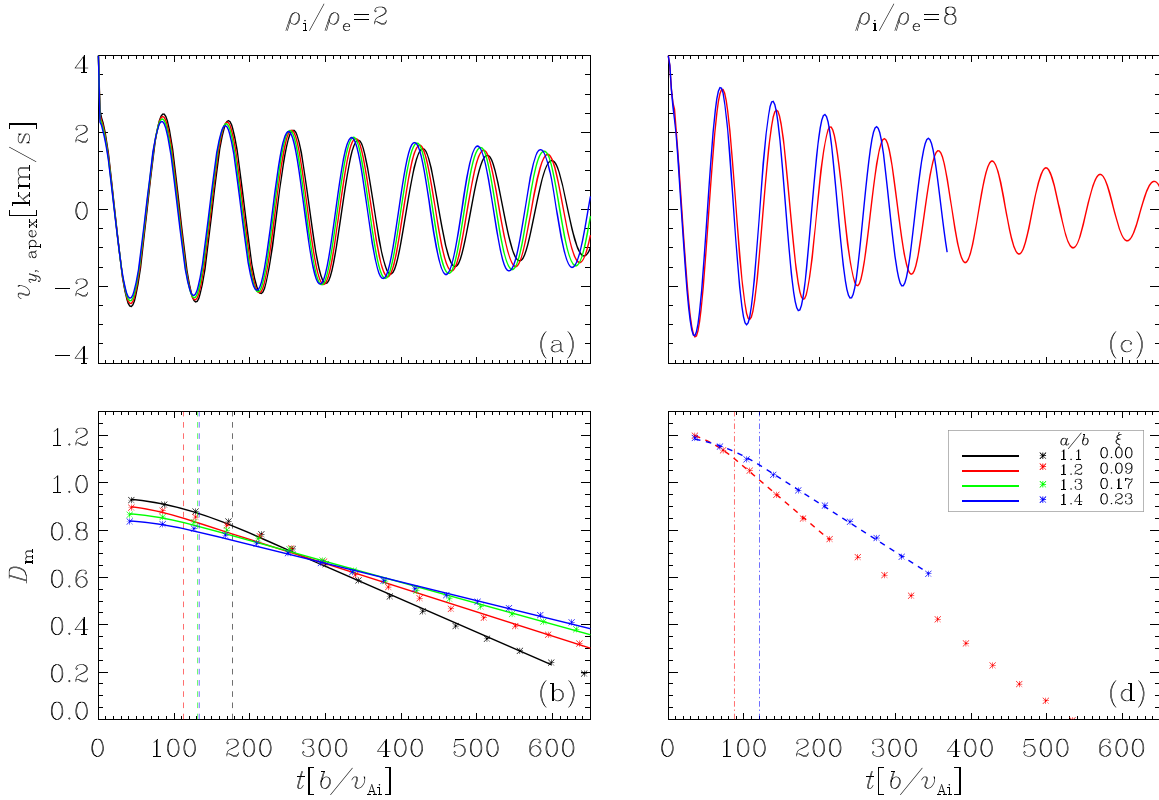
Figure 10. Similar to Figure 9, but for kink oscillations polarized along the minor axis (m-modes), hence the subscripts y in $v_{y,\mathrm{apex}}$ and m in D_{m}.

with a/b, meaning that δ and hence the smallest TL width ($b\delta$ along the direction of the major axis) decrease as well. In fact, this poses a computational issue because a cell size as small as 5 km is necessary for us to resolve the TL for an a/b as modest as 1.4. We therefore choose not to increase a/b any more.

In addition to varying a/b, we will also experiment with two choices of the density ratio $\rho_{\mathrm{i}}/\rho_{\mathrm{e}}$, one being 2 and the other being 8. These two choices are not arbitrary. Rather, they are intended to bring out the different behavior of the damping times (τ) as expected with Equation (A5). Note that Equation (A4) suggests that, at any given $a/b > 1$, the period of the M-mode (P_{M}) always exceeds that of the m-mode (P_{m}) for any $\rho_{\mathrm{i}}/\rho_{\mathrm{e}}$. However, one may readily show that when a/b is given, τ_{m} is longer than τ_{M} when $\rho_{\mathrm{i}}/\rho_{\mathrm{e}} \lesssim 5$, whereas the opposite is true when $\rho_{\mathrm{i}}/\rho_{\mathrm{e}} \gtrsim 5$. To see this, we note that Equation (A5) leads to

$$\frac{\tau_{\mathrm{m}}}{\tau_{\mathrm{M}}} = \left(\frac{a}{b}\right)\left[\frac{1 + (a/b)(\rho_{\mathrm{e}}/\rho_{\mathrm{i}})}{(a/b) + (\rho_{\mathrm{e}}/\rho_{\mathrm{i}})}\right]^{3/2}. \qquad (\mathrm{A6})$$

Suppose for now a/b exceeds unity by only a small amount ε ($0 < \varepsilon \ll 1$). Taylor-expanding the right-hand side of Equation (A6) and retaining only terms that are first order in ε, one finds that

$$\frac{\tau_{\mathrm{m}}}{\tau_{\mathrm{M}}} \approx 1 + \varepsilon\frac{5 - \rho_{\mathrm{i}}/\rho_{\mathrm{e}}}{2 + \rho_{\mathrm{i}}/\rho_{\mathrm{e}}}. \qquad (\mathrm{A7})$$

It then follows that the behavior of $\tau_{\mathrm{m}}/\tau_{\mathrm{M}}$ changes when $\rho_{\mathrm{i}}/\rho_{\mathrm{e}}$ exceeds some critical value ($(\rho_{\mathrm{i}}/\rho_{\mathrm{e}})_{\mathrm{c}}$), which is 5 for an a/b not substantially different from unity. Some further numerical

evaluation demonstrates that $(\rho_{\mathrm{i}}/\rho_{\mathrm{e}})_{\mathrm{c}}$ weakly increases with a/b, becoming 5.7 for an a/b as large as 3.

What difference do we expect regarding our numerical results relative to the analytical ones given by R03, accepting that $\delta/s_0 = 0.1$ is sufficiently small to satisfy the TB approximation? This should come from three sources. First, the plasma β in our simulations is not zero, whereas a zero-β MHD is adopted by R03 from the outset. Nonetheless, the largest β, a fixed value attained at the loop axis (β_{i}), is merely 0.043. Second, the largest a/L we examine will be $1.5b/L = 1.5/50$, which seems to be sufficiently small. Third, we will derive the periods (P) and damping times (τ) largely by applying a fitting procedure to the relevant time series. As such, some uncertainty may arise from the grid resolution and the temporal spacing between the output data slices. However, we have experimented with different choices for these aspects to ensure that the derived values for P and τ converge. All in all, this means that these derived values can be considered to agree with the expectations from R03 if the relative difference is of the order of β_{i}.

We start with a description of the M-modes. The upper row of Figure 9 presents the temporal evolution of the x-component of the velocity at the loop apex ($v_{x,\mathrm{apex}} \equiv v_x(0, 0, L/2; t)$) for two density ratios, one being $\rho_{\mathrm{i}}/\rho_{\mathrm{e}} = 2$ (left column) and the other being 8 (right column). A number of aspect ratios are examined, as represented by the different colors shown in Figure 9(a). From the time series for each combination of $[a/b, \rho_{\mathrm{i}}/\rho_{\mathrm{e}}]$, we extract the extrema $v_{x,\mathrm{apex}}^{\mathrm{extr}}$ and define the damping envelope (D_{M}) as the natural logarithms of their absolute values. This discrete series, represented by the asterisks, is fitted with the three-parameter model as given by Equation (6) in the text to distinguish a Gaussian stage from an exponential one. The best-fit model is then plotted with a dashed curve. In addition, the switch time t_{s} between these two stages is represented by

the vertical dashed–dotted line. The extrema, best-fit curves, and switch times are all given in the lower row and color coded according to a/b in a way consistent with the upper row. When performing the fitting procedure, we exclude the extrema for the initial time interval of the order of the transverse Alfvén time. As explained in the text, this time interval is likely to be connected with the impulsive leaky phase and therefore irrelevant for our further analyses (Terradas et al. 2006b).

Figure 10 presents, in a form identical to Figure 9, the relevant results for the m-modes. A cursory comparison between Figures 9 and 10, the lower rows in particular, indicates that the periods and damping times are different for the M- and m-modes, and this difference depends on the density ratio. This difference will be examined shortly. For now it suffices to note that be it the M- or the m-modes, the impulsive leaky phase is less clear for the larger density ratio, resulting in an oscillation of a larger magnitude in the first couple of cycles. This is expected, given that a larger density ratio makes the coronal loop more efficient in trapping the energy imparted by the initial perturbation. More importantly, the lower rows of Figures 9 and 10 indicate that a Gaussian stage can in general be distinguished from an exponential one, as happens for the profile examined in the text, even though a different transverse density distribution is adopted.

Figure 11 summarizes our examination of the kink oscillations pertinent to the density profile adopted by R03. Here as in the main text, the periods are found by first averaging the temporal spacing between two adjacent extrema in the interval where we perform the fitting procedure, and then multiplying this average by two. These periods (P, Figure 11(a)), together with the damping times in the Gaussian stage (τ^G, Figure 11(b)) and the exponential stage (τ^E, Figure 11(c)), are plotted against a/b as circles (diamonds) for the M-modes (m-modes). In addition, the analytical results expected by R03 (Equations (A4) and (A5)) are given by the solid (dashed) curves for the M-modes (m-modes) as well. Given the lack of analytical results for the damping times in the Gaussian stage, no curves appear in Figure 11(b). Different colors are adopted for different density ratios, as shown in Figure 11(c). Note that the curves for τ^E start with an a/b of 1.1 rather than 1. This is not to say that, in the limit of $a/b \rightarrow 1$, Equation (A5) does not converge to the well-known TTTB result for loops with circular cross sections (given by, e.g., Equation (6) in Goossens et al. 2002). Rather, that TTTB result can be readily recovered if we insist on adopting an a/b-independent δ, in which case δ translates into the ratio between the TL width and the loop radius for a circular cross section. When one chooses to fix δ/s_0, as we do because of computational concerns, δ diverges because s_0 diverges when a/b approaches unity. We choose not to examine this situation. On the other hand, δ does not appear in the expressions for P in the TTTB limit, allowing us to plot P for the entire range of a/b.

Comparing the curves and symbols in Figures 11(a) and (c), one sees that the analytical results in R03 are quantitatively reproduced. Regarding the periods (P), our numerical results agree with R03 in reproducing the tendency for P_M (P_m) to increase (decrease) with a/b, and the tendency for the departure of P_M from P_m to be stronger for a larger ρ_i/ρ_e. Regarding the damping times in the exponential stage (τ^E), one sees that the analytically expected behavior for both τ_M^E and τ_m^E to increase with a/b is reproduced. Note that this behavior is not to be confused with Figure 5 in R03. When translating the damping rate into the damping time, that figure suggests that while τ_M^E tends to increase monotonically with a/b, τ_m^E depends on a/b in
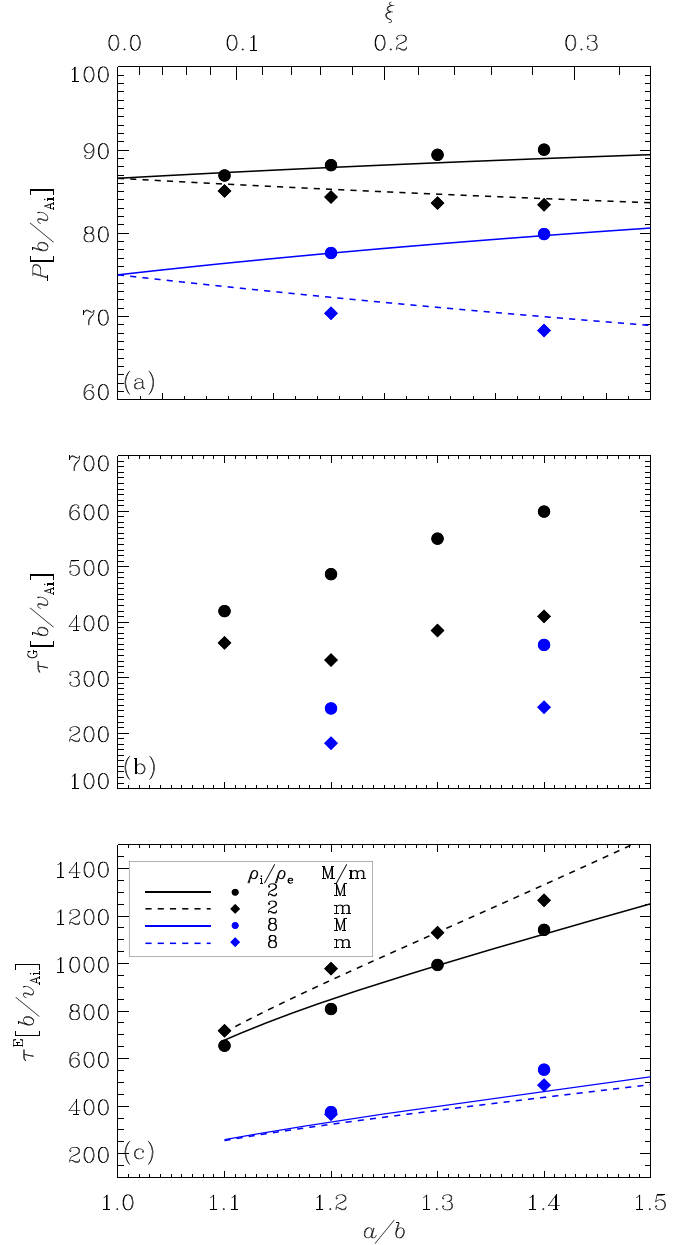

Figure 11. Dependence on the aspect ratio (a/b) of (a) the periods (P) and (b, c) damping times (τ^G, τ^E) of the kink oscillations supported by loops with elliptic cross sections and linear transverse profiles described by Equation (A3). Two different density ratios are examined, as labeled by the different colors. The symbols represent the values found via best fitting our numerical results. We use circles and diamonds to represent the M- and m-modes, respectively. The curves represent the analytical expectations (Equations (A4) and (A5)) from the eigenmode analysis by Ruderman (2003), where the damping times pertain to the exponential stage. We adopt the solid and dashed curves to represent the M- and m-modes, respectively. For validation purposes, the parameter δ/s_0 rather than δ itself is fixed (see the appendix text for details). Note that the flattening $\xi = 1 - b/a$ labeled here represents the deviation of a cross section from a circular one.

a nonmonotonic manner. The reason for this difference is once again our choice of fixing δ/s_0 rather than δ, which in turn is due to concerns of computational cost. With δ/s_0 fixed and s_0 decreasing with a/b, the dependence on a/b in our Figure 11(c) is strengthened relative to Figure 5 in R03. Regardless of the way of specifying δ, the curves in Figure 11(c) indicate that $\tau_M^E < \tau_m^E$ for $\rho_i/\rho_e = 2$, whereas this tendency is reversed when $\rho_i/\rho_e = 8$. This is expected with Equation (A7). It is just that τ_M^E is very
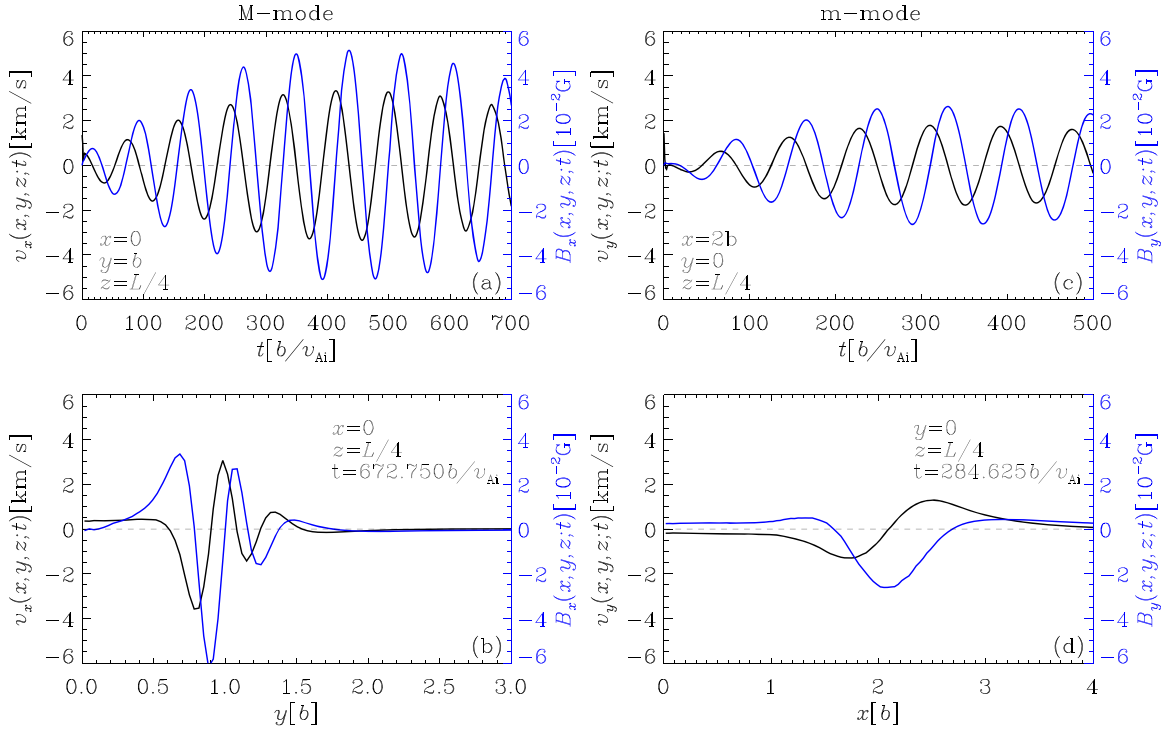
Figure 12. Spatial and temporal distributions of the relevant component of the velocity (black curves) and magnetic field vectors (blue), sampled to examine the M-mode (left column) and m-mode (right column) kink oscillations in a loop with a density contrast $\rho_i/\rho_e = 2$ and an aspect ratio $a/b = 2$. Among the full set of spatial and temporal coordinates, only one is allowed to vary in each panel, whereas the remaining ones are fixed as given by the numbers. This loop pertains to the equilibrium configuration examined in the main text.

close to τ_m^E for $\rho_i/\rho_e = 8$. This latter behavior is also expected, for Equation (A6) suggests that τ_m^E/τ_M^E becomes essentially independent of ρ_i/ρ_e when ρ_i/ρ_e becomes sufficiently large. Despite the minor difference between the symbols and the curves in blue, our numerical results nonetheless capture this ρ_i/ρ_e-insensitivity for a sufficiently large ρ_i/ρ_e. Without the necessary analytical results to compare with, the symbols in Figure 11(b) are given to simply restate that a Gaussian damping envelope can be found in addition to an exponential one even with the profile adopted by R03. Furthermore, one thing irrespective of how δ is specified is that the values for τ^G for the M-modes tend to exceed the ones for the m-modes for both density ratios, which is at variance with the behavior of τ^E.

Appendix B
Resonant Conversion of Kink Oscillations into Alfvén Modes

We have argued that the apparent damping of the kink oscillations is due to their resonant conversion into Alfvén modes in the inhomogeneous layer surrounding the loop boundary. While this argument is physically intuitive, some further support seems desirable to make it more concrete. For this purpose, we will choose a number of representative loops that have been examined in the main text. In addition, let us recall that the loops are primarily characterized by the density contrast ρ_i/ρ_e and the major-to-minor-half-axis ratio a/b.

We start by shedding some light on the nature of the enhanced oscillations in the inhomogeneous layer pertaining to a loop with $\rho_i/\rho_e = 2$ and $a/b = 2$. This loop is chosen because the corresponding M-mode (m-mode) has been detailed in Figures 3 and 4 (Figures 6 and 7). It suffices to examine the M-mode for now, for which the left column of

Figure 12 presents some detailed behavior of the x-component of the velocity (v_x, black curves) and magnetic field (B_x, blue). Figure 12(a) samples both quantities at a fixed location of $[x, y, z] = [0, b, L/4]$, while Figure 12(b) provides a snapshot for both variables at $t = 672.75 \, b/v_{Ai}$ sampled at $[x, z] = [0, L/4]$. From Figure 12(a) one sees that both v_x and B_x grow almost immediately after the impulsive leaky phase. After a couple of cycles, v_x tends to lead B_x by $\pi/2$. In addition, Figure 12(a) indicates that a similar phase difference exists between the y-distributions of the two quantities as well. This phase difference is a strong indication of the Alfvénic nature of the sampled oscillatory signals. To see this, recall that only linear perturbations are of interest in the present study, and that our equilibrium magnetic field $\boldsymbol{B}_0$ is in the z-direction. Recall further that the transverse structuring of our equilibrium quantities is realized through $\bar{r}$ (see Equation (2)). It then follows that, in the $x = 0$ plane, the x-direction is perpendicular to both $\boldsymbol{B}_0$ and the direction of inhomogeneity (the y-direction). Linear Alfvén waves in this case are well known to be governed by (e.g., Heyvaerts & Priest 1983)

$$\frac{\partial v_x}{\partial t} = \frac{B_0(y)}{\mu_0 \rho_0(y)} \frac{\partial B_x}{\partial z}, \tag{B1}$$

$$\frac{\partial B_x}{\partial t} = B_0(y) \frac{\partial v_x}{\partial z}. \tag{B2}$$

Given the boundary conditions, one readily finds that one solution to Equations (B1) and (B2) reads as

$$v_x(y, z; t) = \mathcal{C}(y) v_A(y) \sin[k_z v_A(y) t] \sin(k_z z), \tag{B3}$$

$$B_x(y, z; t) = -\mathcal{C}(y) B_0(y) \cos[k_z v_A(y) t] \cos(k_z z), \tag{B4}$$

where $k_z = \pi/L$ is the axial wavenumber, and the y-dependence of the amplitude function $\mathcal{C}(y)$ is in principle arbitrary at
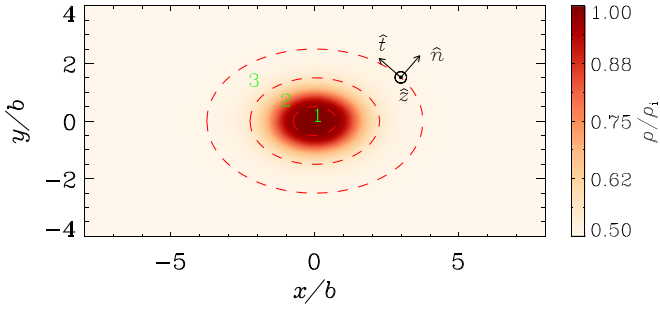
Figure 13. Illustration of the coordinate system employed to examine the energetics of the loop system. Shown for reference is the xy-distribution of the equilibrium density for a loop with a density contrast $\rho_i/\rho_e = 2$ and an aspect ratio $a/b = 1.5$. This loop pertains to the equilibrium configuration examined in the main text. The intersection of any magnetic surface with the x–y plane is an ellipse and can be labeled by the dimensionless variable $\bar{r}$ (see Equation (2)). In the x–y plane, the unit vectors normal and tangential to a magnetic surface are denoted by $\hat{n}$ and $\hat{t}$, respectively. For later use, three regions are distinguished as enclosed by a selected number of magnetic surfaces shown by the dashed curves. The outer boundaries of regions 1–3 correspond to $\bar{r} = 0.5$, 1.5, and 2.5, respectively. The inhomogeneity of the equilibrium parameters is contained in region 2 only.

this point. Evidently, this solution represents an axial fundamental mode, and therefore v_x leads B_x by $\pi/2$ for a given pair of $[y, z]$ when $0 < z < L/2$. Our numerical results are consistent with this expectation. In fact, the reason that we have chosen to sample the signals somewhere between the footpoint ($z = 0$) and apex ($z = L/2$) is to make sure that v_x and B_x are both finite for ease of presentation. Furthermore, it turns out that the spatial dependence of the Alfvén speed $v_A(y)$ (or rather $v_A(\bar{r})$) in the inhomogeneous layer is not far from a linear one. On top of that, the envelope $\mathcal{C}(y)$ varies on a spatial scale larger than the layer width. It then follows from Equations (B3) and (B4) that $v_x(y)$ leads $B_x(y)$ by roughly $\pi/2$ at some given $[x, z; t]$ when $0 < z < L/2$. Note that the particular form in Equations (B3) and (B4) is an indication that these linear Alfvén waves are connected to the kink oscillations. After all, that they appear as an axial fundamental derives from the imposed z-dependence of our velocity driver. We note further that the y-dependence of v_A is responsible for the phase mixing of the resonantly converted Alfvén waves, an effect well known since Heyvaerts & Priest (1983; see also Kaneko et al. 2015 for the consequences of phase mixing). However, when moving away from the $x = 0$ plane, the Alfvénic nature of the enhanced oscillations cannot be revealed in a similar manner. Rather, it can be discerned from the close resemblance of the flow pattern presented in Figure 3 to the $m = 1$ Alfvén waves (Spruit 1982, Figure 1) in loops with circular cross sections, even though we have examined coronal loops with elliptic cross sections and hence the azimuthal wavenumber m cannot be unambiguously defined. All of the discussions we have offered apply to the m-mode as well, for which the right column of Figure 12 examines v_y and B_y that are sampled in the $y = 0$ plane.

The resonant conversion of kink oscillations to localized Alfvén modes can also be examined from the energetics perspective. This examination turns out to be nontrivial. We start by noting that it is well established that the total energy density (ϵ) and energy flux density ($\mathbf{f}$) in general do not adequately capture the wave energetics (e.g., Bogdan et al. 2003; Vigeesh
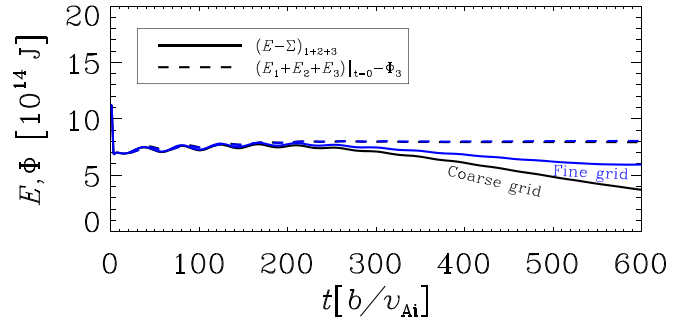

Figure 14. Overall energy balance associated with wave-like perturbations in all three regions in Figure 13. Two computations are examined, one with the reference grid setup adopted in the main text (black curves), the other with a substantially finer grid (blue). The solid curves represent $E - \Sigma$, which characterizes the total energy content. The dashed curves are connected to the outward energy flux leaving the outer boundary of region 3. Here the M-mode oscillation is examined; see Appendix B text for details.

et al. 2009). While some modified ϵ and $\mathbf{f}$ targeting wave-like perturbations have been developed (Wright & Thompson 1994; see also Braginskii 1965; Bray & Loughhead 1974), they suffer from interpretative ambiguities (see Section 4 in Bogdan et al. 2003 for a detailed discussion) and need to be extended for the equilibrium configuration examined in this study. We choose to start directly from the linearized ideal MHD equations by maintaining mathematical consistency at this stage, and we leave more insightful physical interpretations for a future study.

A conservation law can be readily found for linear wave-like perturbations,

$$\frac{\partial \epsilon}{\partial t} = -\nabla \cdot \mathbf{f} + s, \qquad (B5)$$

where ϵ and $\mathbf{f}$ represent some wave-related energy and energy flux densities, respectively. Defined by

$$\epsilon = \frac{1}{2}\rho_0 \delta v^2 + \frac{\delta \mathbf{B}^2}{2\mu_0} + \frac{(\delta p)^2}{2\gamma p_0}, \qquad (B6)$$

$$\mathbf{f} = \delta p \delta \mathbf{v} + \frac{\delta \mathbf{B} \times (\delta \mathbf{v} \times \mathbf{B}_0)}{\mu_0}, \qquad (B7)$$

they agree with the well-known expressions offered in, say, Bogdan et al. (2003). Here the symbols with a δ represent the small-amplitude perturbations to the equilibrium and can be explicitly written as $\delta p(\mathbf{x}; t) = p(\mathbf{x}; t) - p_0(\mathbf{x})$, $\delta \mathbf{v}(\mathbf{x}; t) = \mathbf{v}(\mathbf{x}; t)$, and $\delta \mathbf{B}(\mathbf{x}; t) = \mathbf{B}(\mathbf{x}; t) - \mathbf{B}_0(\mathbf{x})$. Different from the well-known results is some source term

$$s = \frac{1}{\mu_0}[(\nabla \times \mathbf{B}_0) \times \delta \mathbf{B}] \cdot \delta \mathbf{v} - \frac{\delta p \delta \mathbf{v} \cdot \nabla \ln p_0}{\gamma}. \qquad (B8)$$

Evidently, s arises only for nonuniform equilibria. To be more precise, it is relevant only in those portions of an equilibrium where the equilibrium quantities are not uniform. From the energetics perspective, it also makes sense to integrate Equation (B5) over some volume V, the result being

$$\frac{d}{dt}\int_V \epsilon \, dV = -\oint_{\partial V} d\mathbf{A} \cdot \mathbf{f} + \int_V s \, dV, \qquad (B9)$$

where ∂V is the surface that encloses V. In addition, the surface integral collects the net flux that leaves the volume.
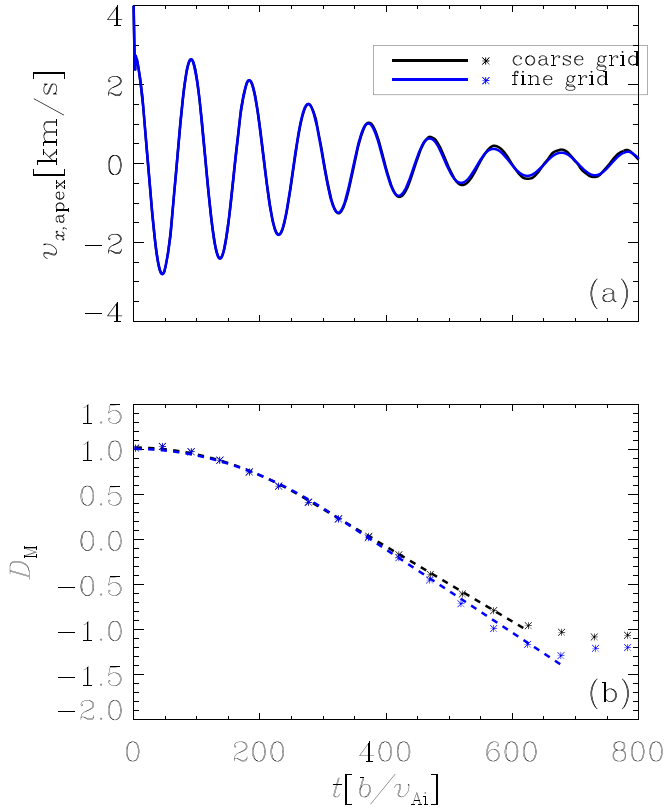
19

Figure 15. Similar to Figure 2, but for an M-mode kink oscillation in a loop with $a/b = 1.5$ and $\rho_i/\rho_i = 2$. The black curves here are reproduced from the curves pertinent to $a/b = 1.5$ shown in Figure 2, while the blue lines represent a fine-grid simulation.

Given our equilibrium configuration, one naturally chooses a volume V to be a straight cylinder that is concentric with the loop and is bounded by the planes $z = 0$ and $z = L$. With our boundary conditions at the bounding planes, it can be readily shown that f_z vanishes therein, and hence the net flux in Equation (B9) derives only from the lateral surface of the volume V. Physically speaking, this lateral surface is a magnetic surface, namely where the Alfvén speed v_A or equivalently $\bar{r}$ is constant (see Equation (3)). For mathematical convenience, we then introduce a new coordinate system $(\bar{r}, \phi)$ in the x–y plane such that the Cartesian coordinates (x, y) of any point can be expressed by

$$x = a\bar{r}\cos\phi, \quad y = b\bar{r}\sin\phi, \quad (B10)$$

where ϕ ranges between 0 and 2π. Note that this ϕ does not have the same meaning as in a standard cylindrical coordinate system. Regardless, the unit vector $\hat{n}$ normal to a magnetic surface can be readily evaluated as

$$\hat{n} = \frac{b\cos\phi\hat{x} + a\sin\phi\hat{y}}{\sqrt{a^2\sin^2\phi + b^2\cos^2\phi}}. \quad (B11)$$

This unit vector is shown in Figure 13, together with the unit vector tangential to a magnetic surface $(\hat{t})$ and the spatial distribution of the equilibrium density ρ_0 in the x–y plane. Note that the ellipses in Figure 13 correspond to a selected number of magnetic surfaces. To evaluate the integrals in Equation (B9), we note further that the line elements in the
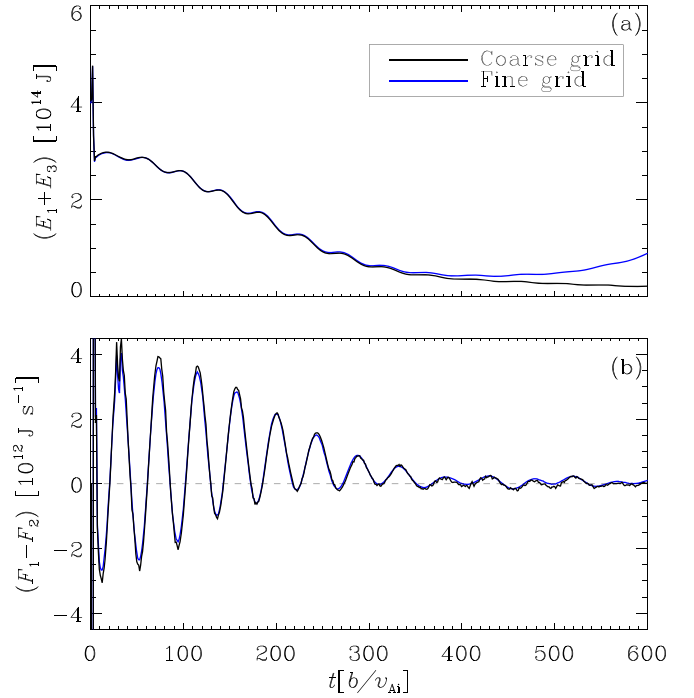

Figure 16. Energy balance associated with wave-like perturbations in the three regions in Figure 13. Shown here are the temporal profiles of (a) the total energy in regions 1 and 3, and (b) the net energy flux injected into region 2. Here the M-mode oscillation is examined; see Appendix B text for details.

$\hat{t}$- and $\hat{n}$-directions (dl_t and dl_n) read as

$$dl_t = \sqrt{a^2\sin^2\phi + b^2\cos^2\phi}\,(\bar{r}d\phi), \quad (B12)$$

$$dl_n = \frac{ab}{\sqrt{a^2\sin^2\phi + b^2\cos^2\phi}}d\bar{r}. \quad (B13)$$

Now labeling the lateral surface of the volume with $\bar{r}$, one readily recognizes that

$$\int_V g(x, y, z; t)dV = \int_0^L dz \int_0^{\bar{r}} (ab)\bar{r}'d\bar{r}'$$
$$\times \int_0^{2\pi} g(\bar{r}', \phi, z; t)d\phi, \quad (B14)$$

where g represents both ϵ and s. Likewise, one readily sees that

$$\oint_{\partial V} d\mathbf{A} \cdot \mathbf{f}(x, y, z; t) = \int_0^L dz \int_0^{2\pi} \hat{n} \cdot \mathbf{f}(\bar{r}, \phi, z; t)$$
$$\times \sqrt{a^2\sin^2\phi + b^2\cos^2\phi}\,(\bar{r}d\phi). \quad (B15)$$

With the following definitions,

$$E(\bar{r}; t) = \int_V \epsilon\, dV, \quad S(\bar{r}; t) = \int_V s\, dV,$$
$$\Sigma(\bar{r}; t) = \int_0^t dt' S(\bar{r}; t'),$$
$$F(\bar{r}; t) = \oint_{\partial V} d\mathbf{A} \cdot \mathbf{f}, \quad \Phi(\bar{r}; t) = \int_0^t dt' F(\bar{r}; t'), \quad (B16)$$

it then follows from Equation (B9) that

$$\frac{dE(\bar{r}; t)}{dt} = -F(\bar{r}; t) + S(\bar{r}; t), \quad (B17)$$

or equivalently

$$E(\bar{r}; t) = E(\bar{r}; t = 0) - \Phi(\bar{r}; t) + \Sigma(\bar{r}; t). \quad (B18)$$

To proceed, we rather arbitrarily choose a loop with $\rho_i/\rho_e = 2$ and $a/b = 1.5$ and examine the M-mode only. Shown in Figure 13, three regions in the plane transverse to this loop are distinguished as labeled. Let $\bar{r}_j$ denote the outer boundary of each region ($j = 1, 2, 3$). For ease of description, the following shorthand notations prove helpful:

$$F_j = F(\bar{r}_j; t), \quad \Phi_j = \Phi(\bar{r}_j; t), \quad (B19)$$

which pertain to the energy flux leaving the outer boundary of region j. Likewise, we adopt the shorthand notations E_j and Σ_j to denote the contribution to the relevant volume integrals from only region j. Evidently,

$$E_j = E(\bar{r}_j; t) - E(\bar{r}_{j-1}; t),$$
$$\Sigma_j = \Sigma(\bar{r}_j; t) - \Sigma(\bar{r}_{j-1}; t), \quad (B20)$$

when $j = 2, 3$. Furthermore, $E_1 = E(\bar{r}_1; t)$ and $\Sigma_1 = \Sigma(\bar{r}_1; t)$. We choose $\bar{r}_1 = 0.5$ and $\bar{r}_2 = 1.5$ such that the inhomogeneity is essentially present only in region 2 (recall that the nominal loop boundary corresponds to $\bar{r} = 1$). In practice, this means that $\Sigma_j \neq 0$ only when $j = 2$. In addition, we set $\bar{r}_3 = 2.5$ for the following reason. Drawing an analogy to kink oscillations in loops with circular cross sections, one expects that the apparent damping of the kink oscillations in our case is connected to some net energy flow into region 2 (see, e.g., Wright & Thompson 1994; Soler et al. 2013). However, for this to be evaluated more quantitatively, one would require that F_3 be negligible after the kink oscillations have been set up.

Figure 14 examines the temporal evolution of the time-integrated energy flux (Φ_3, the black dashed curve). Note that for ease of presentation, here $E(\bar{r}_3; t = 0) - \Phi(\bar{r}_3; t) = (E_1 + E_2 + E_3)|_{t=0} - \Phi_3$ rather than Φ_3 is plotted. Regardless, the point is that this black dashed curve should become close to a horizontal line provided that F_3 vanishes after the system has evolved for some time (see Equation (B16)). In fact, this expectation takes place almost immediately after the impulsive leaky phase. On top of that, this behavior is true even if we choose a larger value of $\bar{r}_3$, which is nonetheless rather arbitrarily set to 2.5. Figure 14 also shows the temporal evolution of $E(\bar{r}_3; t) - \Sigma(\bar{r}_3; t)$ (black solid curve), which is labeled with a subscript $1+2+3$ because this quantity incorporates the contributions from all three regions. In view of Equation (B18), one expects that the black solid and dashed curves should coincide with each other. This is indeed true for $t \lesssim 280 \, b/v_{Ai}$. In particular, the rapid initial drop in both curves offers a more insightful illustration of the impulsive leaky phase; namely, the total energy in the volume bordered by $\bar{r}_3$ is lost through the outward energy flux. One may then question whether the disagreement between the black solid and dashed curves means that our numerical results are not that trustworthy for large t. We address this issue by performing another numerical run with a substantially finer grid, with the smallest grid size reaching 20 km (600 km) in the x- and y-directions (the z-direction). The corresponding results, plotted by the blue curves, indeed indicate a better agreement between the solid and dashed curves. A relative difference of $\lesssim 25\%$ is seen, which is remarkably good for fully 3D simulations. In

contrast, the relative difference may reach $\sim 50\%$ for the coarse grid, namely the reference grid setup that has been consistently used in the main text.

Now a digression from the energetics is necessary, because one may ask whether the periods and damping times are substantially different for different grid setups. Figure 15 examines the temporal evolution of v_x sampled at the loop apex ($[x, y, z] = [0, 0, L/2]$) by showing both (a) the $v_{x,apex}$ series and (b) its damping envelope (D_M). Comparing the coarse-grid (black curves) results with the fine-grid ones (blue), one discerns some difference only in D_M when $t \gtrsim 400 \, b/v_{Ai}$. We then perform the three-parameter fitting to the fine-grid version of D_M, finding that the period (P) and the damping time in the Gaussian stage (τ^G) differ little from the coarse-grid values. In fact, the damping time in the exponential stage (τ^E) is not that different either. The relative difference is merely 9.8%, which is much smaller than the differences in the relative accuracy regarding the overall energy balance. This means that it is much less numerically demanding for one to capture the characteristic timescales for kink oscillations than to realize a remarkably accurate energy conservation. From this we conclude that the values we derived for τ^E with the reference grid setup are in general trustworthy. On top of that, the derived values for P and τ^G are even more reliable. That said, we note in passing that the fine-grid computation suggests that the irregular oscillations toward the end of the simulations are likely to be primarily of numerical origin. On the one hand, the exponential stage in this case does extend to some longer time than in the coarse-grid case. On the other hand, the accuracy in energy conservation is less good than in the interval where the oscillations are regular.

Now we are ready to examine the energy injection into region 2. For this purpose, we employ the mathematical preparation in Equation (B17) rather than Equation (B18), because the flux F proves more intuitive than its time-integrated counterpart Φ. Figure 16 examines both (a) the total energy ($E_1 + E_3$) in regions 1 and 3 and (b) the energy flux ($F_1 - F_2$) injected into region 2 . The reason for us to examine the energy in regions 1 and 2 is that the source term S vanishes therein. As has been pointed out, the definition of E, which derives from the definition of the energy density ϵ (Equation (B6)), does not suffer any interpretive ambiguity. However, while mathematically consistent, the source term needs to be interpreted in a more physical manner. Leaving this aspect to a future dedicated study, we note that the rate of decrease (increase) of $E_1 + E_2$ is expected to be balanced by a positive (negative) $F_1 - F_2$ after the impulsive leaky phase. Figure 16 indicates that this expectation is indeed valid. In particular, the overall loss of the wave energy in regions 1 and 2 is due to a net positive ($F_1 - F_2$), thereby making it more concrete to conclude that the energy associated with the kink oscillation is resonantly absorbed somewhere in the inhomogeneous layer. We note that the oscillatory behavior at half the kink period, which is particularly pronounced in Figure 16(b), arises because we are evaluating second-order quantities (see Equations (B6) and (B7)). In addition, the fine-grid results (blue curves) are inconsistent with the coarse-grid ones only when t exceeds, say, $\sim 400 \, b/v_{Ai}$. We have argued that this does not mean that the characteristic timescales we have derived with the reference grid setup are not trustworthy.

ORCID iDs

Mingzhe Guo ⓘ https://orcid.org/0000-0003-4956-6040
Bo Li ⓘ https://orcid.org/0000-0003-4790-6718
Tom Van Doorsselaere ⓘ https://orcid.org/0000-0001-9628-4113

References

Afanasyev, A. N., Van Doorsselaere, T., & Nakariakov, V. M. 2020, A&A, 633, L8
Andries, J., Arregui, I., & Goossens, M. 2005, ApJL, 624, L57
Andries, J., Van Doorsselaere, T., Roberts, B., et al. 2009, SSRv, 149, 3
Anfinogentov, S., Nisticò, G., & Nakariakov, V. M. 2013, A&A, 560, A107
Anfinogentov, S. A., & Nakariakov, V. M. 2019, ApJL, 884, L40
Anfinogentov, S. A., Nakariakov, V. M., & Nisticò, G. 2015, A&A, 583, A136
Antolin, P., De Moortel, I., Van Doorsselaere, T., & Yokoyama, T. 2016, ApJL, 830, L22
Antolin, P., Okamoto, T. J., De Pontieu, B., et al. 2015, ApJ, 809, 72
Arregui, I., Andries, J., Van Doorsselaere, T., Goossens, M., & Poedts, S. 2007, A&A, 463, 333
Arregui, I., & Goossens, M. 2019, A&A, 622, A44
Aschwanden, M. J. 2009, SSRv, 149, 31
Aschwanden, M. J. 2011, LRSP, 8, 5
Aschwanden, M. J., Fletcher, L., Schrijver, C. J., & Alexander, D. 1999, ApJ, 520, 880
Aschwanden, M. J., Nakariakov, V. M., & Melnikov, V. F. 2004, ApJ, 600, 458
Aschwanden, M. J., Nightingale, R. W., Andries, J., Goossens, M., & Van Doorsselaere, T. 2003, ApJ, 598, 1375
Aschwanden, M. J., & Schrijver, C. J. 2011, ApJ, 736, 102
Banerjee, D., Erdélyi, R., Oliver, R., & O'Shea, E. 2007, SoPh, 246, 3
Bogdan, T. J., Carlsson, M., Hansteen, V. H., et al. 2003, ApJ, 599, 626
Braginskii, S. I. 1965, RvPP, 1, 205
Bray, R. J., & Loughhead, R. E. 1974, The Solar Chromosphere (London: Chapman and Hall)
Browning, P. K., & Priest, E. R. 1984, A&A, 131, 283
Chen, S.-X., Li, B., Xiong, M., Yu, H., & Guo, M.-Z. 2015, ApJ, 812, 22
De Moortel, I., & Nakariakov, V. M. 2012, RSPTA, 370, 3193
De Moortel, I., & Pascoe, D. J. 2009, ApJL, 699, L72
Duckenfield, T. J., Goddard, C. R., Pascoe, D. J., & Nakariakov, V. M. 2019, A&A, 632, A64
Dymova, M. V., & Ruderman, M. S. 2006, A&A, 457, 1059
Edwin, P. M., & Roberts, B. 1983, SoPh, 88, 179
Erdélyi, R., & Morton, R. J. 2009, A&A, 494, 295
Erdélyi, R., & Taroyan, Y. 2008, A&A, 489, L49
Goddard, C. R., Nisticò, G., Nakariakov, V. M., & Zimovets, I. V. 2016, A&A, 585, A137
Goossens, M., Andries, J., & Aschwanden, M. J. 2002, A&A, 394, L39
Goossens, M., Arregui, I., Ballester, J. L., & Wang, T. J. 2008, A&A, 484, 851
Goossens, M., Erdélyi, R., & Ruderman, M. S. 2011, SSRv, 158, 289
Goossens, M., Soler, R., Terradas, J., Van Doorsselaere, T., & Verth, G. 2014, ApJ, 788, 9
Guo, M., Van Doorsselaere, T., Karampelas, K., et al. 2019a, ApJ, 870, 55
Guo, M., Van Doorsselaere, T., Karampelas, K., & Li, B. 2019b, ApJ, 883, 20
Guo, Y., Erdélyi, R., Srivastava, A. K., et al. 2015, ApJ, 799, 151
Heyvaerts, J., & Priest, E. R. 1983, A&A, 117, 220
Hillier, A., Barker, A., Arregui, I., & Latter, H. 2019, MNRAS, 482, 1143
Hollweg, J. V., & Yang, G. 1988, JGR, 93, 5423
Hood, A. W., Ruderman, M., Pascoe, D. J., et al. 2013, A&A, 551, A39
Howson, T. A., De Moortel, I., Antolin, P., Van Doorsselaere, T., & Wright, A. N. 2019, A&A, 631, A105
Ionson, J. A. 1978, ApJ, 226, 650
Kaneko, T., Goossens, M., Soler, R., et al. 2015, ApJ, 812, 121
Karampelas, K., Van Doorsselaere, T., & Antolin, P. 2017, A&A, 604, A130
Klimchuk, J. A., Antiochos, S. K., & Norton, D. 2000, ApJ, 542, 504
Kucera, T. A., Young, P. R., Klimchuk, J. A., & DeForest, C. E. 2019, ApJ, 885, 7
López Fuentes, M. C., Klimchuk, J. A., & Démoulin, P. 2006, ApJ, 639, 459
Magyar, N., & Nakariakov, V. M. 2020, ApJL, 894, L23

Magyar, N., & Van Doorsselaere, T. 2016, A&A, 595, A81
Malanushenko, A., & Schrijver, C. J. 2013, ApJ, 775, 120
McLaughlin, J. A., & Ofman, L. 2008, ApJ, 682, 1338
Mignone, A., Bodo, G., Massaglia, S., et al. 2007, ApJS, 170, 228
Morton, R. J., & Ruderman, M. S. 2011, A&A, 527, A53
Nakariakov, V. M., Anfinogentov, S. A., Nisticò, G., & Lee, D. H. 2016a, A&A, 591, L5
Nakariakov, V. M., & Ofman, L. 2001, A&A, 372, L53
Nakariakov, V. M., Ofman, L., Deluca, E. E., Roberts, B., & Davila, J. M. 1999, Sci, 285, 862
Nakariakov, V. M., Pilipenko, V., Heilig, B., et al. 2016b, SSRv, 200, 75
Nakariakov, V. M., & Verwichte, E. 2005, LRSP, 2, 3
Nechaeva, A., Zimovets, I. V., Nakariakov, V. M., & Goddard, C. R. 2019, ApJS, 241, 31
Nisticò, G., Nakariakov, V. M., & Verwichte, E. 2013, A&A, 552, A57
Ofman, L., & Wang, T. J. 2008, A&A, 482, L9
Pascoe, D. J., Anfinogentov, S. A., Goddard, C. R., & Nakariakov, V. M. 2018, ApJ, 860, 31
Pascoe, D. J., & De Moortel, I. 2014, ApJ, 784, 101
Pascoe, D. J., Goddard, C. R., & Nakariakov, V. M. 2016a, A&A, 593, A53
Pascoe, D. J., Goddard, C. R., Nisticò, G., Anfinogentov, S., & Nakariakov, V. M. 2016b, A&A, 585, L6
Pascoe, D. J., Goddard, C. R., Nisticò, G., Anfinogentov, S., & Nakariakov, V. M. 2016c, A&A, 589, A136
Pascoe, D. J., Hood, A. W., de Moortel, I., & Wright, A. N. 2012, A&A, 539, A37
Pascoe, D. J., Hood, A. W., De Moortel, I., & Wright, A. N. 2013, A&A, 551, A40
Pascoe, D. J., Hood, A. W., & Van Doorsselaere, T. 2019, FrASS, 6, 22
Reale, F. 2014, LRSP, 11, 4
Roberts, B. 2000, SoPh, 193, 139
Ruderman, M. S. 2003, A&A, 409, 287
Ruderman, M. S. 2009, A&A, 506, 885
Ruderman, M. S. 2015, SoPh, 290, 423
Ruderman, M. S., & Roberts, B. 2002, ApJ, 577, 475
Ruderman, M. S., & Roberts, B. 2006, JPlPh, 72, 285
Ruderman, M. S., & Terradas, J. 2013, A&A, 555, A27
Schrijver, C. J., DeRosa, M. L., & Title, A. M. 2010, ApJ, 719, 1083
Selwa, M., & Ofman, L. 2010, ApJ, 714, 170
Selwa, M., Ofman, L., & Solanki, S. K. 2011a, ApJ, 726, 42
Selwa, M., Solanki, S. K., & Ofman, L. 2011b, ApJ, 728, 87
Soler, R., Goossens, M., Terradas, J., & Oliver, R. 2013, ApJ, 777, 158
Soler, R., Goossens, M., Terradas, J., & Oliver, R. 2014, ApJ, 781, 111
Soler, R., & Terradas, J. 2015, ApJ, 803, 43
Spruit, H. C. 1982, SoPh, 75, 3
Terradas, J., Oliver, R., & Ballester, J. L. 2006a, ApJL, 650, L91
Terradas, J., Oliver, R., & Ballester, J. L. 2006b, ApJ, 642, 533
Tian, H., McIntosh, S. W., Wang, T., et al. 2012, ApJ, 759, 144
Tomczyk, S., & McIntosh, S. W. 2009, ApJ, 697, 1384
Tomczyk, S., McIntosh, S. W., Keil, S. L., et al. 2007, Sci, 317, 1192
Van Doorsselaere, T., Andries, J., Poedts, S., & Goossens, M. 2004, ApJ, 606, 1223
Van Doorsselaere, T., Nakariakov, V. M., Young, P. R., & Verwichte, E. 2008, A&A, 487, L17
Van Doorsselaere, T., Verwichte, E., & Terradas, J. 2009, SSRv, 149, 299
Verth, G., & Erdélyi, R. 2008, A&A, 486, 1015
Verwichte, E., Aschwanden, M. J., Van Doorsselaere, T., Foullon, C., & Nakariakov, V. M. 2009, ApJ, 698, 397
Verwichte, E., Nakariakov, V. M., Ofman, L., & Deluca, E. E. 2004, SoPh, 223, 77
Verwichte, E., Van Doorsselaere, T., White, R. S., & Antolin, P. 2013, A&A, 552, A138
Vigeesh, G., Hasan, S. S., & Steiner, O. 2009, A&A, 508, 951
Wang, F., Deng, H., Li, B., et al. 2018, ApJL, 856, L16
Wang, H., & Sakurai, T. 1998, PASJ, 50, 111
Wang, T., Ofman, L., Davila, J. M., & Su, Y. 2012, ApJL, 751, L27
Wang, T. J. 2016, GMS, 216, 395
Wentzel, D. G. 1979, ApJ, 227, 319
White, R. S., & Verwichte, E. 2012, A&A, 537, A49
Wright, A. N., & Thompson, M. J. 1994, PhPl, 1, 691
Zimovets, I. V., & Nakariakov, V. M. 2015, A&A, 577, A4